TITLE

Interactions between the N- and C- termini of mechanosensitive ion channel AtMSL10 support a three-step mechanism for activating its signaling function

AUTHORS/AFFILIATIONS

Debarati Basu[1], Jennette M. Shoots[1], Alex Harkess[2], Kira M. Veley[2] and Elizabeth S. Haswell[1]

[1]NSF Center for Engineering Mechanobiology, Dept. of Biology, Washington University in St. Louis, St. Louis MO 63130, [2]Donald Danforth Plant Science Center, St. Louis, Missouri 63132.

CONTACT INFORMATION

ehaswell@wustl.edu

RUNNING TITLE

Interaction between the N- and C-termini of MSL10

ABSTRACT

Although a growing number of mechanosensitive ion channels are being identified in plant systems, the molecular mechanisms by which they function remain to be established. Overexpression of the mechanosensitive ion channel MSL (MscS-Like)10 fused to GFP triggers a number of developmental and cellular phenotypes including the induction of cell death, and this function is regulated by seven phosphorylation sites in its soluble N-terminus. Here, we show that these and other phenotypes required neither overexpression nor a tag and could be also induced by a point mutation in the soluble C-terminus (S640L). In all cases, these gain-of-function phenotypes were suppressed by growth at elevated temperatures. The promotion of cell death and hyperaccumulation of H_2O_2 in *35S:MSL10*^{S640L}*-GFP* overexpression lines was suppressed by N-terminal phosphomimetic substitutions, and the soluble N- and C-terminal domains of MSL10 physically interacted. Finally, transcriptomic analysis revealed that the complex network of genes induced by these gain-of-function *MSL10* alleles overlap with established biotic and abiotic stress-responsive pathways. We propose a three-step model by which tension-activated conformational changes in the C-terminus activate the N-terminus, leading to its dephosphorylation and the induction of adaptive responses. Taken together, this work expands our understanding of the molecular mechanisms of mechanotransduction in plants.

KEYWORDS

MscS-Like, MSL10, mechanosensitive ion channel, cell death, reactive-oxygen species

INTRODUCTION

Mechanical forces, whether endogenous or exogenous in origin, are important stimuli that help direct plant growth, development, and immune responses. External mechanical perturbations include touch, wounding, wind, vibration, gravity, osmotic stress, and pathogen invasion (Monshausen and Haswell, 2013; Jayaraman et al., 2014). Endogenous mechanical forces include turgor pressure, a fundamental cue influencing cell expansion (Hamant and Haswell, 2017; Kierzkowski, 2019). Before plants can coordinate a cellular response to these varied stimuli, they must be able to precisely sense and transduce mechanical cues.

Mechanosensitive (MS) ion channels provide a fast and efficient molecular mechanism for transducing mechanical stimuli into intracellular signals. They are found in all domains of life, and are highly diverse in terms of their structure, ion selectivity, regulation, and physiological roles (Martinac et al., 2013; Ranade et al., 2015; Basu and Haswell, 2017). However, all MS ion channels share two common attributes: opening in response to mechanical force (lateral membrane tension, forces relayed from the cytoskeleton, or a combination of both) and facilitating the passive flow of ions across membrane (Bavi et al., 2017).

In plants, there is a growing list of predicted and established MS ion channel families, which includes the MscS-Like (MSL, Basu and Haswell, 2017), Two Pore Potassium (TPK, Maathuis, 2011), Mid1-Complementing Activity (MCA, Nakagawa et al., 2007) and Reduced Hyperosmolality-induced [Ca^{2+}] Increase (OSCA, (Hou et al., 2014; Yuan et al., 2014; Murthy et al., 2018) families, as well as homologs of the animal MS ion channel Piezo (Zhang et al., 2019). Plant MS channels have been implicated in a wide range of physiological functions, including organellar osmoregulation (Veley et al., 2012), stomatal closure (Gobert et al., 2007; Yuan et al., 2014), cold tolerance (Mori et al., 2018), hyperosmolarity-evoked Ca^{2+} influx (Yuan et al., 2014), penetration of hard substrates (Nakagawa et al., 2007), pathogen-triggered immunity (Zhang et al., 2017) and viral resistance (Zhang et al., 2019). However, the detailed molecular mechanisms by which MS channels participate in these events need further investigation.

The MSL family of MS ion channels was first identified based on homology to the canonical MS ion channel from *Escherichia coli,* Mechanosensitive ion channel of Small conductance (*Ec*MscS)

66 (Pivetti et al., 2003; Haswell and Meyerowitz, 2006; Haswell et al., 2008). There are ten MSLs
67 encoded in the *Arabidopsis thaliana* genome, and they are localized to mitochondria (MSL1, Lee
68 et al., 2016), to chloroplasts (MSL2/3, Haswell and Meyerowitz, 2006) or to the plasma membrane
69 (MSL8, MSL9 and MSL10, Haswell et al., 2008; Hamilton et al., 2015). The tension-gated ion
70 flux of MSL1, MSL8, and MSL10 have been examined by single channel patch-clamp
71 electrophysiology (Maksaev and Haswell, 2012; Hamilton et al., 2015; Lee et al., 2016).
72 MSL2/MSL3 and MSL8 are thought to serve as osmotic safety valves in plastids and in pollen,
73 respectively (Veley et al., 2012; Hamilton et al., 2015). MSL1 plays a poorly understood role
74 maintaining redox homeostasis in mitochondria (Lee et al., 2016).
75
76 While MSL10 was the first in the family to be characterized by electrophysiology, its physiological
77 function is still under study. To date, no visible loss-of function phenotypes have been reported in
78 *msl10-1* null mutants (nor in double *msl9-1 msl10-1* mutants, where MSL10's closest homolog
79 MSL9 is also ablated). Overexpression of *MSL10-GFP* results in growth retardation, ectopic cell
80 death, constitutive production of H_2O_2, and induction of genes involved in ROS accumulation,
81 senescence, and abiotic and biotic stress responses (Veley et al., 2014). These gain-of-function
82 phenotypes can be attributed to a single domain of MSL10, the soluble N-terminus; in a transient
83 *Nicotiana benthamiana* expression system, this domain can induce cell death on its own (Veley et
84 al., 2014). In another study, we showed that variants of MSL10-GFP harboring pore-blocking
85 lesions also induce cell death in this system (Maksaev et al., 2018). None of the phenotypes
86 associated with *MSL10-GFP* overexpression are observed in plants overexpressing a version of
87 *MSL10-GFP* harboring four phospho-mimetic substitutions in the N-terminus (*MSL10* $^{S57D, S128D,}$
88 $^{S131E, T136D}$*-GFP*, or *MSL10*^{4D}*-GFP)*, though this variant has MS ion channel activity, protein levels,
89 and subcellular localization indistinguishable from the wild type.
90
91 Thus, dephosphorylation of the MSL10 N-terminus activates *MSL10-GFP* to trigger cell death
92 when overexpressed in Arabidopsis or in *N. benthamiana*. Ion flux through the channel pore,
93 however, is not required. We infer that under normal conditions, MSL10 remains in its inactive
94 state (i.e. with a phosphorylated N-terminus), and that overexpression overwhelms the kinase that
95 normally maintains it in its inactive form, thereby triggering a cell death signaling cascade. It has
96 been shown that the opening of *Ec*MscS is accompanied by structural rearrangement of the soluble

97 C-terminal domain (Bass et al., 2002; Wang et al., 2008; Machiyama et al., 2009; Rowe et al.,
98 2014). If similar rearrangements occur in MSL10, the N-terminus could also undergo tension-
99 induced conformational changes that lead to activation, either directly from the channel pore or
100 indirectly from the C-terminal domain.
101
102 Indeed, a functional link between the N- and the C-termini of MSL10 was suggested by a recent
103 report by the Zhou group (Zou et al., 2015). The *rea1 (RAP2.6 expresser in shoot apex)* mutant
104 harbors an EMS-induced point mutation (S640L) located in the soluble C-terminus of *MSL10* that
105 leads to increased expression of a wound-responsive luciferase reporter gene. Mutant *rea1* plants
106 exhibit growth retardation and ectopic cell death, strikingly reminiscent of *MSL10-GFP*
107 overexpression lines. The *rea1* mutants also exhibited shorter petioles, accumulation of
108 anthocyanin pigments, lack of apical dominance, wound-induced hyperaccumulation of JA, and
109 altered expression of genes involved in JA biosynthesis and response (*LIPOXYGENASE2* or
110 *LOX2*, *PLANT DEFENSIN* or *PDF1.2,* and *ALLENE OXIDASE* or *AOS)*.
111
112 The *rea1* mutant thus provides the opportunity to probe MSL10 function in an endogenous context.
113 Its phenotypic similarity to *MSL10-GFP* overexpression lines suggested that growth retardation,
114 ROS accumulation, and cell death might reflect physiological functions of the MSL10 protein,
115 though it was also possible that these similarities might be only superficial. Here we present an in-
116 depth comparison of the developmental, cellular and gene expression phenotypes resulting from
117 *MSL10-GFP* overexpression, the *rea1* lesion, and genomic phospho-variants of *MSL10*. The
118 results from these experiments prompted us to assess genetic and physical interactions between
119 the soluble N- and C- termini of MSL10 and to characterize the gene expression pattern connecting
120 MSL10 activation to downstream phenotypic effects. Our results suggest a three-step process of
121 MSL10 activation that transduces the effect of increased membrane tension from soluble C-
122 terminus to the N-terminus of the channel, leading to phosphorylation and subsequently triggering
123 downstream gene expression networks.
124
125

126 **RESULTS**

127

128 **Conservation of functionally significant residues in the soluble N- and C-terminal domains**
129 **of putative MSL10 orthologs**

130 We investigated the conservation of eight residues previously identified as important for MSL10
131 function: seven phosphorylation sites in the soluble N-terminus (S29, S46, S48, S57, S128, S131,
132 and T136; and a C-terminal amino acid that is mutated in the *rea1* mutant (S640, Zou et al., 2015)
133 (**Figure 1A**). The predicted N-terminal domains of putative MSL10 homologs from other
134 flowering plants showed surprisingly low sequence conservation. However, when analysis was
135 restricted to the *Brassicacae* family, the 33-amino-acid region containing S29, S46, S48 and S57,
136 and the 15-amino-acid region containing S128, S131, and T136 showed 73% amino acid identity
137 with the *Brassica napus* homolog (**Figure 1B)**. The sequence of the MSL10 C-terminus
138 surrounding S640 was highly conserved among angiosperms (90% amino acid identity with the
139 putative homolog from *B. napus,* 60% identity with that from *Oryza sativa*), and S640 itself was
140 conserved in 11 of the 15 sequences analyzed (**Figure 1C**). To summarize, phosphosites in the
141 soluble N-terminus known to modulate the *MSL10-GFP* overexpression phenotype were not well-
142 conserved, while S640, a residue in the soluble C-terminus known to affect MSL10 function, was
143 well-conserved among the sequences analyzed.

144

145 ***rea1* is a recessive gain-of-function *MSL10* allele, renamed *msl10-3G***

146 To further characterize the *rea1* allele, we backcrossed *rea1* plants to wild type *Col-0* plants. As
147 shown in **Figure S1A**, the resulting F1 hybrid plants resembled the wild type parent, indicating
148 that the mutation responsible for the phenotypes observed in the *rea1* mutant is recessive,
149 consistent with previous findings (Zou et al., 2015). After self-pollination, the resulting F2
150 population segregated into wild-type and *rea1* phenotypes at a ratio of 3:1, as expected for a
151 recessive allele, and these results were confirmed by PCR genotyping (**Figure S1C**). In addition,
152 *rea1* plants were outcrossed to *msl10-1* null mutant plants. The F1 progenies resembled *rea1* in
153 terms of leaf morphology but attained intermediate height after 8 weeks of growth (**Figure S1B**).
154 After self-pollination, resulting F2 populations similarly segregated approximately 1:2:1 with
155 respect to height at late stages of development (wild type like: intermediate: *rea1* phenotype);
156 phenotypes were confirmed by PCR genotyping (**Figure S1C**). These data show that the

157 phenotypic effects of the *rea1* lesion depend on the presence or absence of the WT *MSL10* allele,
158 suggest that they may be dosage-dependent (as it requires two copies of the *rea11* mutant allele to
159 generate the full *rea1* phenotype), and confirm that the phenotypes associated with the *rea1* mutant
160 are due to a recessive gain-of-function point mutation in the *MSL10* gene. This allele is hereafter
161 called *msl10-3G*.
162
163 ***MSL10-GFP* overexpression, the *msl10-3G* allele, and the *MSL10g^{7A}* transgene produce**
164 **similar phenotypes and gene expression patterns**
165 Strong constitutive overexpression of a gene often results in pleiotropic phenotypes that may not
166 reflect its normal function (Zhang et al., 2003a; Kovalchuk et al., 2013), and the addition of tags
167 can alter protein localization, regulation, stability or function (Spartz et al., 2012). Zou et al. (2015)
168 reported that neither estradiol-induced expression of *MSL10-FLAG* nor constitutive expression of
169 untagged *MSL10* resulted in the phenotypes seen with constitutive expression of *MSL10-GFP*,
170 suggesting that large tags may perturb the function of MSL10. Furthermore, we were previously
171 unable to retrieve plants constitutively expressing *MSL10^{4A}–GFP* (Veley et al., 2014), and while
172 we proposed that the over-expression of phospho-dead *MSL10* was lethal, it remained possible that
173 an unrelated defect in the transgene prevented us from isolating any transgenic plants.
174
175 To determine if the phenotypes associated with *MSL10-GFP* overexpression could be replicated
176 at endogenous expression levels and without a GFP tag, we generated constructs to drive
177 expression of untagged wild-type *MSL10 (MSL10g)*, phospho-dead *MSL10* S29A, S46A, S48A,
178 S57A, S128A, S131A, and T136A (*MSL10g^{7A}*) or phospho-mimetic *MSL10* S29D, S46D, S48D,
179 S57D, S128D, S131E, and T136D (*MSL10g^{7D}*), within the native *MSL10* genomic context. These
180 constructs were introduced into the *msl10-1* null mutant background and three independent
181 homozygous transgenic lines from each transformation that accumulated *MSL10* transcripts at
182 levels similar or slightly higher than those of wild-type plants (**Figure S2A**) were selected for
183 further analysis.
184

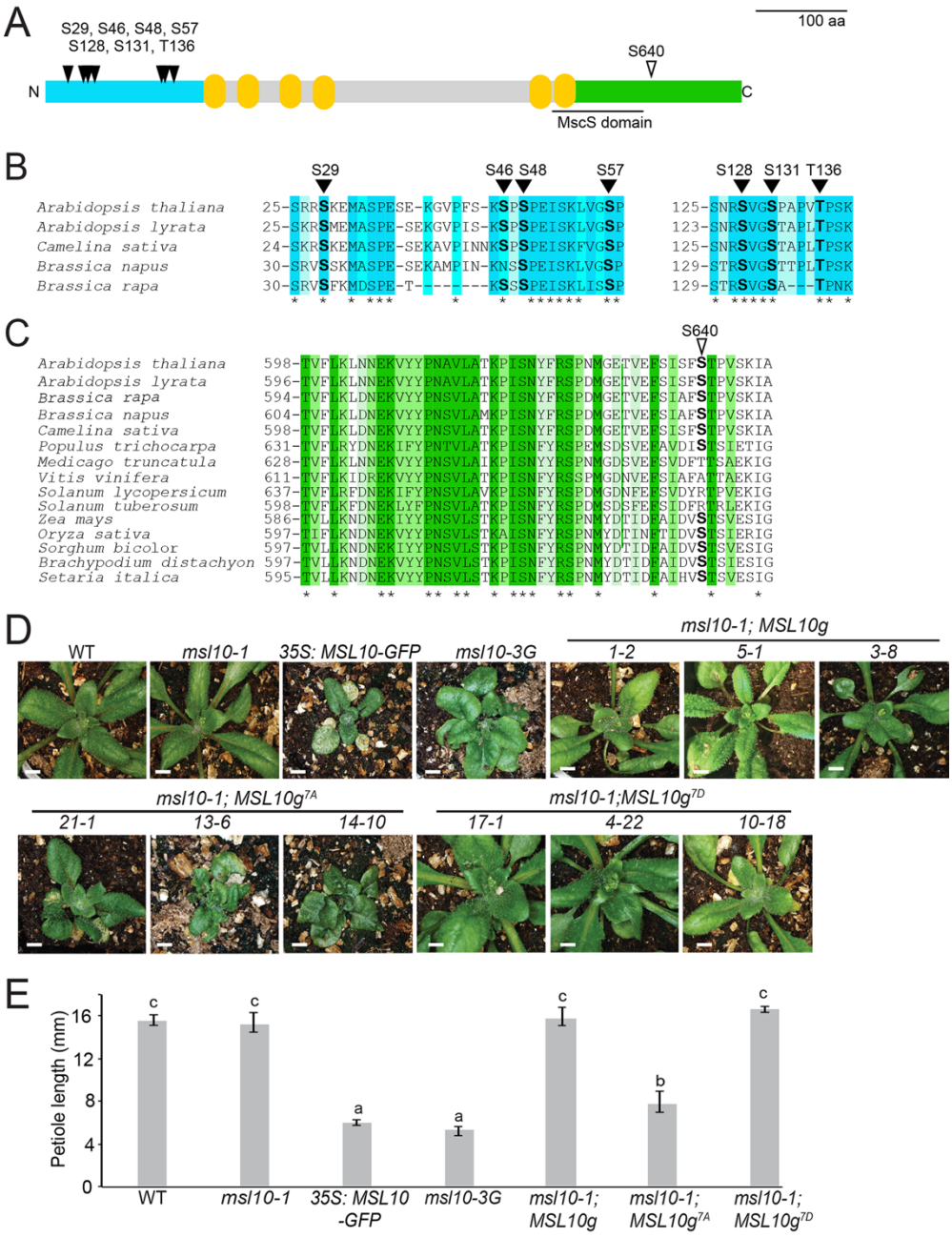

Figure 1. *MSL10-GFP* overexpression lines, *msl10-3G* mutants, and *MSL10g^{7A}* lines have similar whole-plant phenotypes. (A) Predicted topology of an AtMSL10 monomer. Teal, cytosolic N-terminus; yellow, transmembrane helices; green, cytosolic C-terminus. Black triangles denote the positions of the residues mutated in this study. The MscS domain is as defined in (Veley et al. 2014). (B) Multiple alignment of protein sequences corresponding to the N-terminus of putative AtMSL10 orthologs in the Brassicaceae family. Darker teal shading indicates higher conservation score and identical amino acids with an asterisk. (C) Multiple alignment of protein sequences corresponding to the C-terminus of putative AtMSL10 orthologs in selected flowering plants. Conservation of residues is indicated as in (B). (D) and (E) T4 homozygous lines overexpressing *MSL10-GFP* in the Col-0 background (line 15-2), T3 homozygous lines expressing *MSL10g*, or *MSL10g^{7D}* in the *msl10-1* background, and T3 segregating or T3 homozygous lines expressing *MSL10g^{7A}* in the *msl10-1* background were selected for comparison. (D) Whole-plant images of 25-day-old plants of the indicated genotypes grown side-by-side at 21°C under a 24-h light regime. Bar = 0.5 cm. (E) Petiole length of the fourth or fifth leaf from 28-day-old plants. Different letters indicate significant differences as determined by one-way ANOVA followed by Tukey's post-hoc test ($P < 0.05$). Error bars indicate ± SD of three replicates (n = 18 per replicate).

185

186 Like the *MSL10-GFP* overexpression lines, the *msl10-3G* mutant and three *MSL10g*^{7A} lines all
187 exhibited reduced rosette size, fresh weight and plant height compared to wild-type (**Figure 1D**,
188 **S2B-D)**. Four- to five-week-old plants from these same lines also exhibited shorter petioles and
189 broader leaf blades compared to wild-type plants (**Figure 1E, S2E-F**). Unlike *MSL10-GFP*
190 overexpression lines, the *msl10-3G* mutant and *MSL10g*^{7A} lines lacked apical dominance (**Figure**
191 **S2G**). The *msl10-1* null mutant and *msl10-1* mutants expressing *MSL10g* or *MSL10g*^{7D} were
192 phenotypically indistinguishable from wild-type plants.
193
194 We next tested if *msl10-3G* mutants, *MSL10*^{7A}*g* lines, and *MSL10-GFP* overexpression lines have
195 similar gene expression patterns. As shown in **Figure 2A**, four genes previously shown to be
196 upregulated in *MSL10-GFP* overexpression lines (*SENESCENCE ASSOCIATED GENE 12*
197 (*SAG12), α-DIOXYGENASE (DOX1), PEROXIDASE-34 (PERX34),* and *OSMOTIN-LIKE*
198 *PROTEIN-34 (OSM34)* (Veley et al., 2014) were also upregulated in *msl10-3G* (4- to 5-fold) and
199 *MSL10g*^{7A} lines (3- to 5-fold) compared to wild-type plants, although not to the same levels as in
200 *MSL10-GFP* overexpression lines (7- to 20-fold). Similarly, four genes previously shown to be
201 upregulated in *rea1* mutants, *LIPOXYGENASE2* (*LOX2*,) *PLANT DEFENSIN* (*PDF1.2), ALLENE*
202 *OXIDASE* (*AOS)* and *RAP2.6* (Zou et al., 2015) were also upregulated in *MSL10-GFP*
203 overexpression lines (14- to 35-fold), and in *MSL10g*^{7A} lines (5- to 12-fold) (**Figure 2B**). Mutant
204 *msl10-1*, *MSL10g*, and *MSL10g*^{7D} lines did not exhibit statistically significant differences in
205 expression of any of these genes compared to wild-type plants. We also observed upregulation of
206 *SAG12, DOX1, OSM34* and *PERX34* and ectopic cell death in response to inducible expression of
207 wild-type and phospho-dead (but not phospho-mimetic) MSL10 (**Figure S3).**
208
209 Thus, overexpression of *MSL10-GFP*, expression of untagged *MSL10*^{7A} at endogenous levels in
210 the *msl10-1* background, and the C-terminal point mutation in the *msl10-3G* allele all lead to
211 growth retardation, defects in petiole length, and the upregulation of eight hallmark genes. While
212 the *MSL10-GFP* overexpression line *15-2* was the most severely affected in all cases, and the only
213 line to display yellowish-brown patches on rosette leaves (**Figure 1D**), all of these phenotypes
214 could be generated to various degrees of severity without overexpression and/or a C-terminal tag,
215 and thus are likely to be related to the normal function of MSL10. Furthermore, these phenotypes
216 are a direct, rather than developmental, effect of ectopic MSL10 activation.

217 We interpret these data to mean that high levels of wild-type MSL10, basal levels of MSL10 that
218 is dephosphorylated at the N-terminus, or basal levels of MSL10 harboring the S640L lesion all
219 lead to a set of pleiotropic phenotypes through the same, as yet unknown, molecular mechanism.
220 We note that a lack of MSL10-specific antibodies prevented us from measuring protein levels in
221 untagged lines, so it is formally possible that MSL10 phospho-dead lesions or the S640L lesion
222 alter protein stability in the absence of a GFP tag. However, these lesions do not alter stability
223 when fused to a GFP tag (see Veley et al., 2014 and **Figure 4B** below).

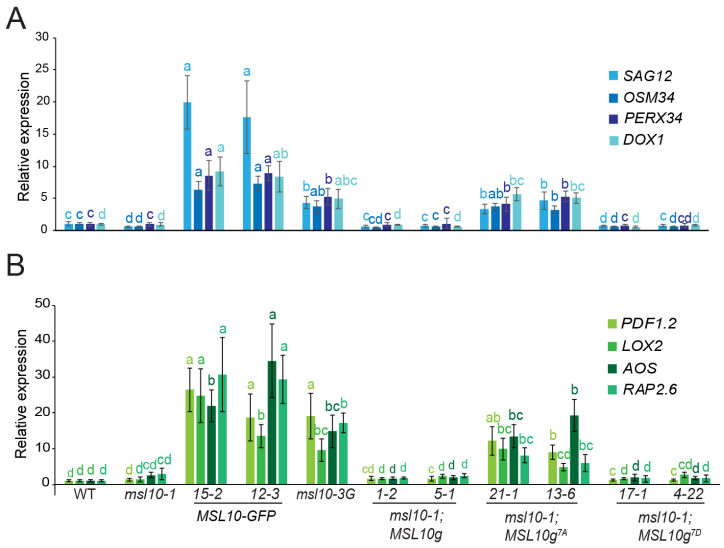

224

Figure 2. *MSL10-GFP* overexpression lines, *msl10-3G* mutants, and *MSL10g^{7A}* lines display similar expression profiles. Quantitative RT-PCR analysis of four genes previously shown to be upregulated in *35S:MSL10-GFP* overexpression lines (A) and four genes previously shown to be upregulated in the *msl10-3G* allele (B). cDNA was synthesized from total RNA extracted from rosette leaves of three-week-old plants grown at 21°C under 24 hours of light. Expression levels of respective genes were normalized to both *EF1α* and *UBQ5*. Mean fold-change values relative to the wild type are plotted, with error bars showing ± SE of the mean of three biological replicates Different letters indicate significant difference as determined by one-way ANOVA followed by Tukey's post-hoc test (P < 0.05). For transgenics, two independent T3 or T4 homozygous lines were selected for comparison.

225 **Growth at high temperatures suppresses phenotypes associated with overexpression of**
226 ***MSL10-GFP*, the *MSL10g^{7A}* lines, and the *msl10-3G* allele**

227 Growth at elevated temperature can ameliorate growth defects and suppress ectopic cell death in
228 a number of mutant backgrounds (Gray et al., 1998; Ichimura et al., 2006; Koini et al., 2009; Quint
229 et al., 2009; Wierzba and Tax, 2016), suggesting that the same might be true for *MSL10-GFP*
230 overexpression. When grown at 30ºC, *MSL10-GFP* overexpressing lines were nearly
231 indistinguishable from wild-type, *msl10-1*, or *msl9-1; msl10-1* plants in terms of rosette size and
232 fresh weight (**Figure 3A** and **S4A**). In these lines, *MSL10* transcript levels were unchanged or only
233 slightly reduced (**Figure 3B**), and neither MSL10-GFP protein abundance nor localization at the
234 periphery of the cell was altered (**Figure 3C** and **S4B**). Thus, growth at high temperatures did not
235 relieve *MSL10-GFP* overexpression-associated phenotypes by altering protein abundance,
236 stability or subcellular localization.

237

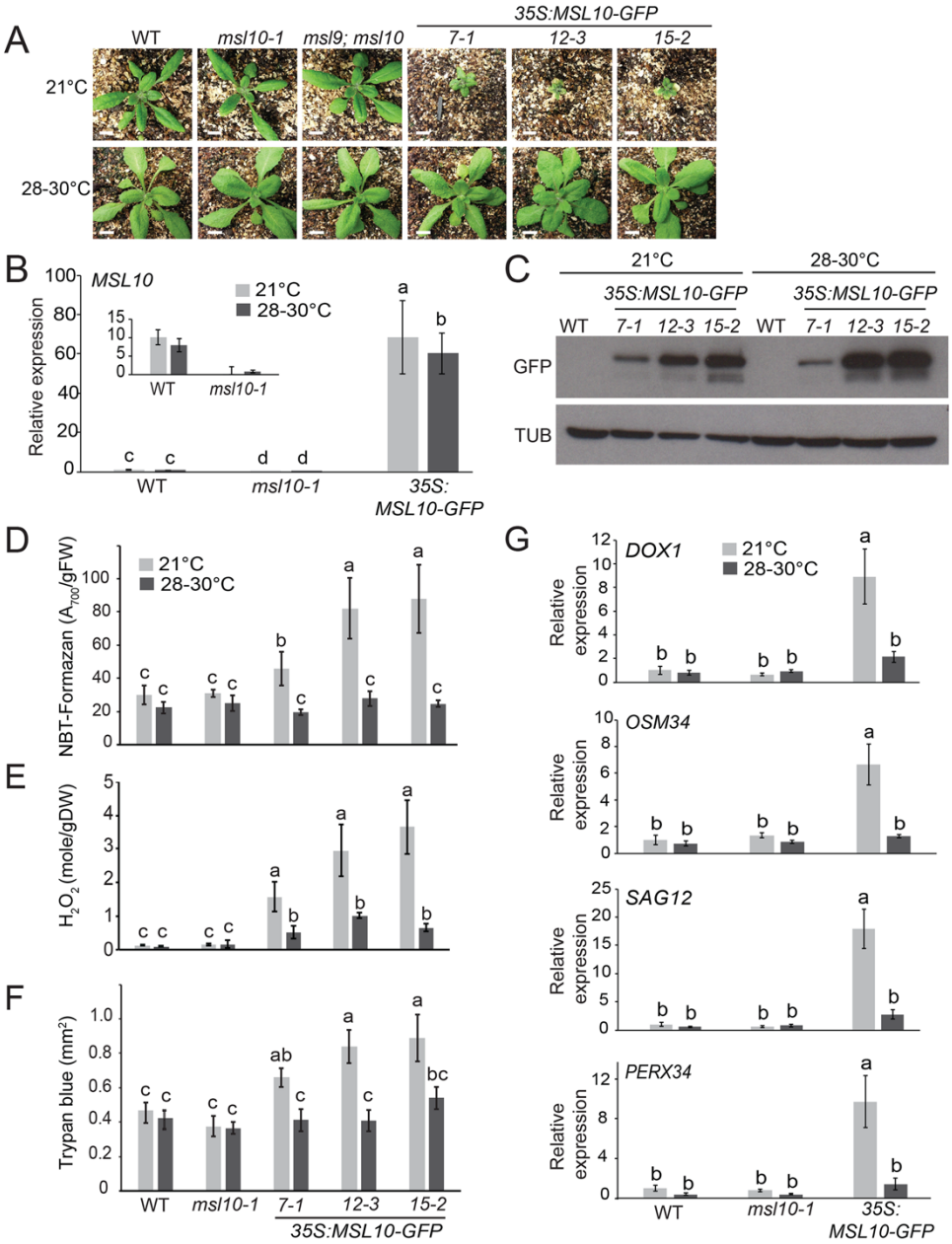

Figure 3. Growth at high temperatures suppresses phenotypes associated with *MSL10-GFP* overexpression. Wild type, *msl10-1*, and three independent T4 homozygous lines overexpressing *MSL10-GFP* in the Col-0 background were grown side-by-side on soil under 24 h light regime and at either 21°C or 28°-30°C. (A) Images of whole three-week-old plants. Bar = 0.5 cm. (B) Relative transcript abundance of *MSL10* analyzed by with qRT-PCR from wild type, *msl10-1*, and *35S:MSL10-GFP* line 15-2. Inset compares *MSL10* expression levels in wild-type and *msl10-1* lines only. (C) Immunoblot analysis of MSL10-GFP levels in rosette leaves of two-week old plants. MSL10-GFP was detected with an anti-GFP primary antibody (top), and then the blot was stripped and re-probed with an anti-α-tubulin primary antibody (bottom). Expected protein sizes are indicated at the left according to a commercially available standard. (D) Colorimetric quantification of NBT-formazan deposition in rosette leaves (see Methods). FW, fresh weight. Data are means ± SD of three replicates (n=18). (E) Hydrogen peroxide (H_2O_2) content, quantified as mmol H_2O_2 per gram dry weight (DW) of rosette leaves using the Amplex Red-coupled fluorescence quantitative assay. Data are means ± SD of three replicates (n=14). (F) Ectopic cell death detected by Trypan blue staining (see Methods). Data are means ± SD of three replicates (n=7-10). (G) Elevation of transcripts in MSL10-GFP overexpression lines is suppressed by high temperature. RNA extraction, cDNA synthesis, and qRT-PCR analyses in (B) and (G) were performed as in Figure 2.

238

239 High temperatures also suppressed the cellular phenotypes of *MSL10-GFP* overexpression lines.
240 Strikingly, levels of O^{2-} (assayed by Nitroblue tetrazolium (NBT); **Figure 3D)**, H_2O_2 (assayed by
241 DAB staining and Amplex Red-coupled fluorescence assay; **Figure 3E**,) and ectopic cell death
242 (assessed by Trypan blue staining; **Figure 3F, S5B**) were strongly suppressed in *MSL10-GFP*
243 overexpression lines grown at high temperatures. In addition, *PERX34, DOX1, OSM34,* and
244 *SAG12* transcript levels in *MSL10-GFP* overexpression lines were reduced to wild-type levels
245 when grown at 28°C-30°C (**Figure 3G)**. We also observed that the growth defects, ROS
246 accumulation and ectopic cell death of lines expressing the $MSL10g^{7A}$ transgene and *msl10-3G*
247 mutants was suppressed when plants were grown at high temperatures (**Figures S5 and S6A-F**).
248 No apparent changes in *MSL10* transcript levels were detected in $MSL10g^{7A}$ or *msl10-3G* lines
249 when grown at high temperature (**Figure S6G**). Taken together, our data show that growth at 28-
250 30°C suppresses all phenotypes associated with the presence of over-active MSL10.
251
252 **Phospho-mimetic lesions in the MSL10 N-terminus suppress *msl10-3G* phenotypes**
253 Given that mutations in the N-terminus ($MSL10g^{7A}$) and the C-terminus (*msl10-3G*) produce
254 similar phenotypes, we tested for a genetic interaction between these two soluble domains. The
255 *msl10-3G* (S640L) mutation was introduced into the *35S:MSL10-GFP* and *35S*:$MSL10^{7D}$*-GFP*
256 transgenes to make $MSL10^{S640L}$*-GFP* and $MSL10^{7D,S640L}$*-GFP*. As expected, overexpression of
257 *MSL10-GFP* and $MSL10^{S640L}$*-GFP* lead to growth retardation, ectopic cell death (as assessed by
258 the occurrence of yellowish-brown lesions on rosette leaves and Trypan blue staining), and
259 enhanced H_2O_2 accumulation in rosette leaves, while overexpression of phospho-mimetic
260 $MSL10^{7D}$*-GFP* did not (**Figure 4A**). $MSL10^{7D,S640L}$*-GFP* plants were indistinguishable from wild
261 type or $MSL10^{7D}$*-GFP* plants. Immunoblotting showed that these phenotypic differences cannot
262 be attributed to differences in protein abundance (**Figure 4B),** and likely reflect the inability of
263 $MSL10^{7D}$-GFP and $MSL10^{7D,S640L}$-GFP to activate downstream signaling. Thus, N-terminal
264 phospho-mimetic substitutions prevent or block the phenotypes produced by the C-terminal lesion
265 S640L found in the *msl10-3G* mutant.
266

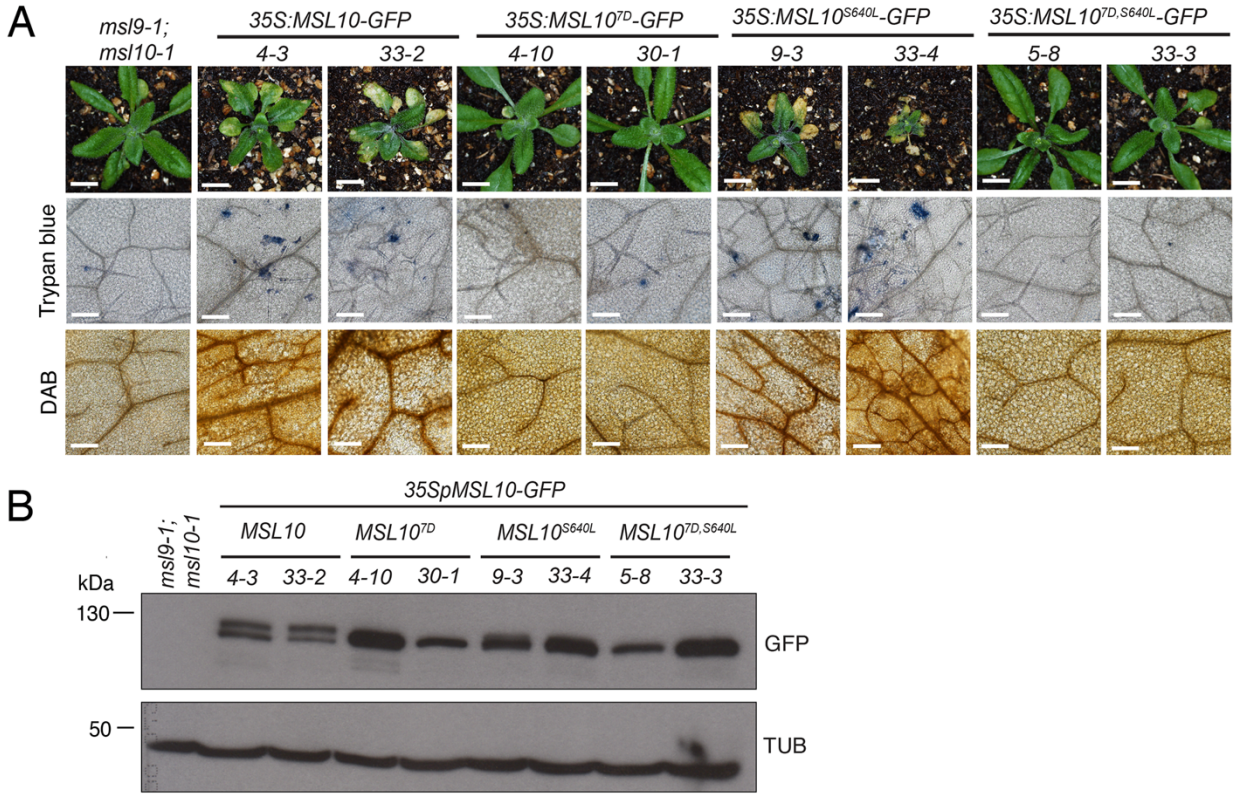

Figure 4. Phospho-mimetic substitutions in the MSL10 N-terminus suppress phenotypes associated with overexpression of MSL10^{S640L}. (A) Top row: Images of three-week-old plants grown at 21°C overexpressing wild-type *MSL10-GFP*, phospho-mimetic *MSL10^{7D}-GFP*, *MSL10^{S640L}-GFP*, or *MSL10^{7D,S640L}-GFP*. Overexpression lines were generated in the *msl9-1;msl10-1* background, phenotypically indistinguishable from *msl10-1*. Two independent homozygous T3 lines for each transgene are shown. Bar = 0.5 cm. Middle row: Trypan blue staining of four-week old leaves from the above T3 plants to visualize ectopic cell death. Bottom row: DAB staining of five-week-old leaves to detect the accumulation of H_2O_2. For leaf images, bar = 0.2 mm. (B) Immunoblot showing that plants harboring various *MSL10-GFP* transgenes accumulate MSL10-GFP to similar levels. Western blot performed as in Figure 3C. The two forms of MSL10-GFP that migrate slower on SDS-PAGE may result from post-translational modifications.

267

268 **The soluble N- and C- termini of MSL10 interact directly in two protein-protein interaction**
269 **assays**

270 To assess whether this genetic interaction between the N- and C-termini of MSL10 might be
271 mediated through physical interactions, we first employed the mating-based split-ubiquitin yeast
272 two-hybrid assay (mbSUS) (Reinders et al., 2002). We previously showed that MSL10 can interact
273 with itself in this assay, but not with close relative MSL9—as expected for a homomeric channel
274 (Veley et al., 2014). We repeated these results and further observed that MSL10 does not interact
275 with an unrelated membrane protein, KAT1 (Obrdlik et al., 2004) (**Figure 5A**).

276

277 To test for interactions specific to the N- and C-termini, we first split MSL10 into two halves, the
278 first comprising the N-terminal domain and the first four TM helices ($MSL10_{1-460}$), and the second
279 comprising the fifth and sixth TM helix as well as the C-terminal domain ($MSL10_{461-734}$). These
280 two halves of MSL10 displayed a strong interaction, providing support for intra- or inter-molecular
281 interactions between different domains of MSL10 (**Figure 5A**). Furthermore, the soluble N-
282 terminus ($MSL10_{1-164}$) and the C-terminal half of MSL10 ($MSL10_{461-734}$) interacted, as did the N-
283 terminal half of MSL10 ($MSL10_{1-460}$) and its soluble C-terminus ($MSL10_{553-734}$). This result
284 suggested that the middle part of the protein—which contains all the TM helices—is not required
285 for self-association. Almost no interaction was detected between the N-terminal half and itself or
286 between the C-terminal half and itself. None of these interactions were affected by the presence of
287 the S640L lesion (indicated as MSL10*).
288
289 To validate these mbSUS interactions, to investigate whether they can occur *in planta*, and to
290 assess interactions without requiring one partner to be tethered to the membrane, we employed a
291 bimolecular fluorescence complementation (BiFC) assay as described in Gehl et al. (2009). The
292 N- and C-terminal halves of YFP (YN- and YC-) were fused to MSL10 variants and transiently
293 expressed in leaf epidermal cells of *Nicotiana benthamiana*. As expected, co-infiltration of
294 MSL10-YN with MSL10-YC resulted in strong YFP signal at the periphery of the cell **(Figure**
295 **5B)**. Strong YFP fluorescence was also detected when $MSL10_{553-734}$-YN was co-infiltrated with
296 $MSL10_{1-164}$-YC (**Figure 5B**) or with $MSL10_{1-460}$-YC (**Figure S7B**). The C-terminal half of MSL10
297 formed aggregates **(Figure S7A**) so we only used the soluble C-terminus ($MSL10_{553-734}$) in this
298 study. Neither the N-terminus nor the C- terminus of MSL10 was able to self-associate in this
299 assay, nor to interact with unfused YN or YC. Furthermore, neither of these domains were able to
300 interact with MSL9 or KAT1 (**Figure 5B, Figure S7B**). Consistent with the mbSUS assay results,
301 the S640L mutation (again indicated as MSL10*) did not affect any interactions; nor did the
302 introduction of phospho-mimetic or phospho-dead lesions into the N-terminal sequences (**Figure**
303 **5B, Figure S7B**). These results demonstrate a direct physical interaction between the soluble N-
304 and C- termini of MSL10 and show that it does not require tethering to the membrane and is
305 unaffected by the S640L lesion or by the phosphorylation status of the N-terminus.
306
307

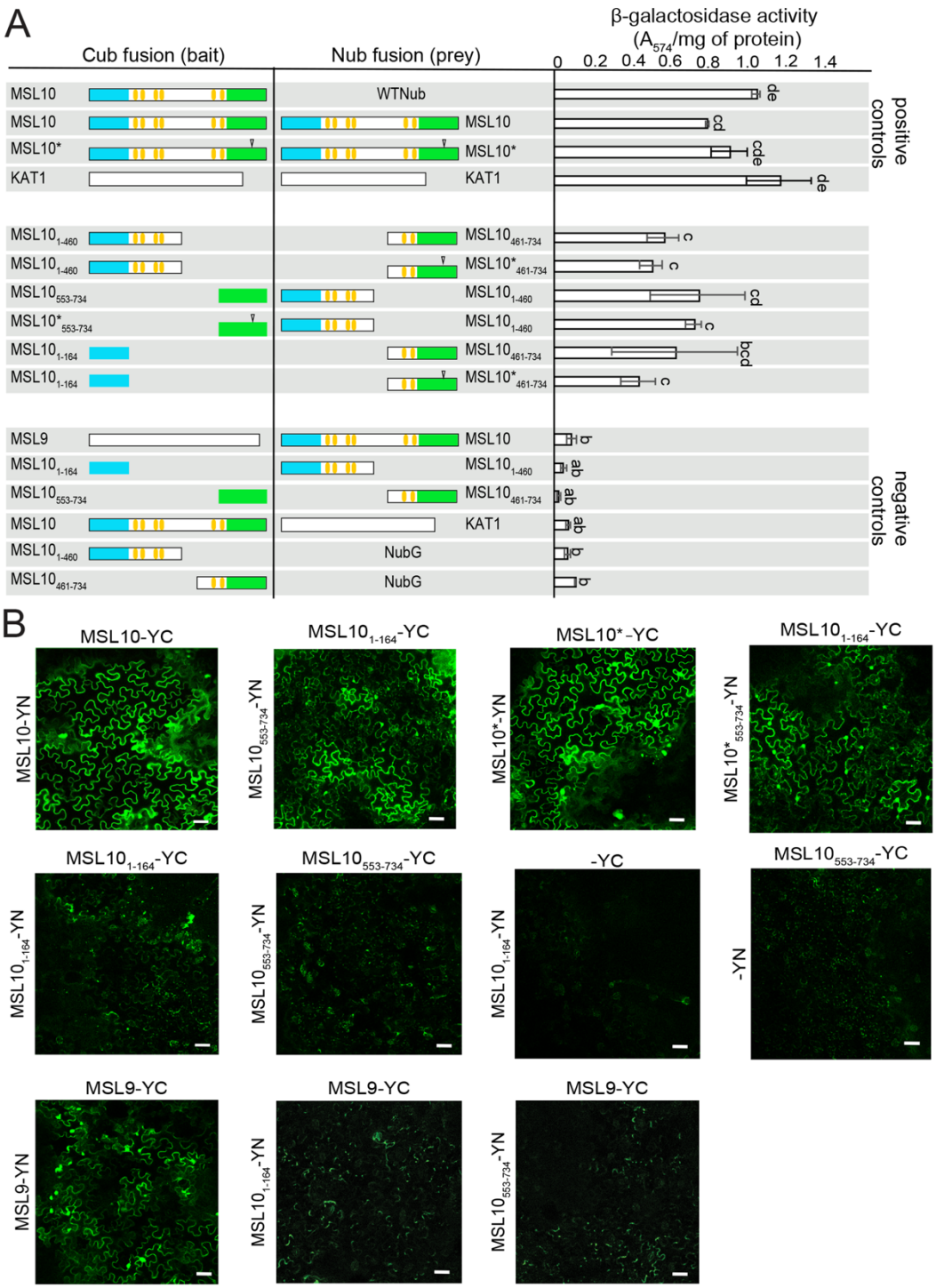

Figure 5. The soluble N- and C- termini of MSL10 interact. (A) Split ubiquitin yeast two-hybrid assay. The strength of interaction between MSL10 truncations was determined in liquid assays (see Methods). The NubWT moiety is used as a positive control. Data presented are means ± SD of three replicates. Different letters indicate significant differences as determined by one-way ANOVA followed by Tukey's post-hoc test ($P < 0.05$). (B) Confocal laser scanning micrographs of the abaxial surface of N. benthamiana leaves 3 to 5 days after infiltration with Agrobacterium harboring the indicated BiFC construct pairs. Scale bar, 50 µm. Identical acquisition settings were used in all images. All experiments were repeated at least three times. MSL10* indicates $MSL10^{S640L}$.

308

309 **A temperature-sensitive gene network induced by *MSL10-GFP* overexpression is associated**
310 **with multiple abiotic and biotic stress responses**
311 To begin to understand the pathways downstream of MSL10 activation, we performed a
312 transcriptome analysis, exploiting the temperature sensitivity of the *35S:MSL10-GFP* phenotype.
313 The workflow is diagrammed in **Figure 6A**. Briefly, wild-type plants and *35S:MSL10-GFP* line
314 *12-3* were grown for three weeks at 21°C, then half of the plants were transferred to 30°C. After
315 24 hours, rosette tissue was collected from duplicate pools, from both genotypes grown under both
316 temperature regimes, resulting in a total of 8 cDNA libraries. An average of 21,910,736 reads were
317 sequenced across all libraries with an average pseudoalignment rate of 95.40%. An assessment of
318 sample clustering using the plotMDS function of edgeR v3.18.1; (Robinson et al., 2010)is shown
319 in **Figure S8A**. A *k*-means clustering analysis was performed across all genotypes and temperature
320 regimes yielded eight distinct clusters with unique response patterns. 'Cluster 2' comprised genes
321 upregulated in the *MSL10-GFP* overexpression line at 21°C, but not at 30°C, and not in wild-type
322 plants at either temperature (**Figure 6B, Table S2**). All eight marker genes upregulated in *MSL10*
323 gain-of-function mutants shown in **Figure 3** were present in Cluster 2 (**Figure S8B**), providing
324 some validation for our procedure.
325
326 Next, the 5828 unique differentially expressed genes in Cluster 2 were subjected to a gene ontology
327 (GO) search using an overrepresentation test (PANTHER 14.1; Mi et al., 2017) and a total of 139
328 GO terms were found (**Table S3)**. The top seven significantly overrepresented GO terms with a p-
329 value cut-off of p=E-25, ranked by their *p*-values, are shown in **Figure 6C.** All seven categories
330 concern the response to environmental stresses of various types, including chemicals and other
331 organisms. Other biological processes such as 'response to acid chemical' 'cellular catabolic
332 process' and 'multi-organism process' were also enriched.
333
334 To identify candidate genes for further validation, and to see if a similar expression pattern was
335 observed in transgenic *MSL10*^{7A}*g* plants and *msl10-3G* mutants, we selected five candidate genes
336 which satisfied the following three criteria: 1) is one of the top 100 genes identified in **Table S2**
337 (highlighted in yellow) that was differentially expressed in *MSL10-GFP* overexpression lines at
338 low temperatures with a threshold filter value >10, 2) belongs to at least two of the overrepresented
339 GO terms shown in **Figure 6C** when these top 100 genes were subject to GO analysis, and 3) there

340 was minimal difference in the threshold value between the two biological replicates (**Table S4**).
341 We measured expression of these five genes (*SENESCENCE ASSOCIATED GENE* (*SAG13*),
342 *LIPOXYGENASE3* (*LOX3*), *TRICHOME BIREFRINGENCE-LIKE 8* (*TBL8*), *ABA-INDUCED*
343 *PP2C GENE-1* (*PP2C-1*) and *ELICITOR-ACTIVATED GENE 3-2* (*ELI3-2*)) in all *MSL10* gain-
344 of-function lines. All five genes were expressed at levels 75- to 150-fold higher in the *MSL10-*
345 *GFP* overexpression line than in the wild type, and a similar upregulation of these genes was
346 displayed in *msl10-3G* (30- to 72-fold) and *MSL10g*^{7A} lines (30- to 62-fold) compared to wild-type
347 plants (**Figure 6D**). In contrast, *msl10-1*, *MSL10g*, and *MSL10g*^{7D} lines did not exhibit detectable
348 changes in expression of any of these genes. These data validate the RNA-Seq analysis and provide
349 both a list of candidate marker and a starting point for a better understanding of the pathways that
350 lead to the phenotypic defects associated with *MSL10* activation. Finally, these results provide
351 further evidence that all the three *MSL10* gain-of-function alleles have similar signaling outputs.
352

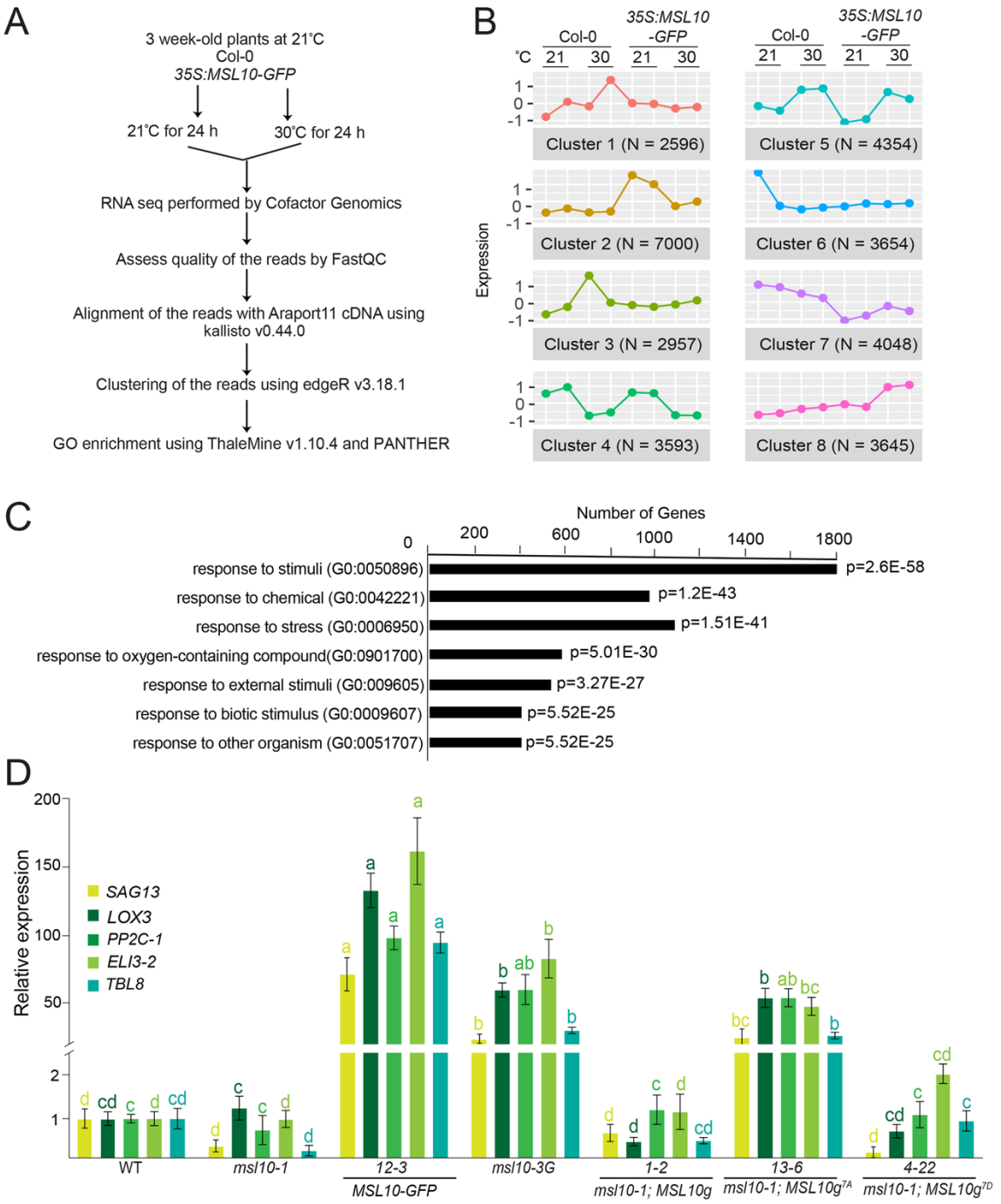

Figure 6. Transcriptome profiling identifies downstream genes associated with *MSL10* gain-of-function lines. (A) Overview of our experimental approach. (B) Averaged expression profiles of gene clusters were identified by centroid based k-means clustering using a K-means function in R. The $\log_2$-transformed expression levels are plotted on the y-axis and samples with biological replicates on the x-axis. (C) The top seven Gene Ontology classes of genes belonging to Cluster 2 as determined through the PANTHER statistical overrepresentation test. The number of genes corresponding to each overrepresented GO term and its associated p values are shown. (D) Five genes selected from the *MSL10-GFP* overexpression RNA-Seq Cluster 2 were upregulated in *MSL10-GFP* overexpression lines, the *msl10-3G* mutant, and lines expressing the *MSL10g*^{7A} transgene. RNA extraction, cDNA synthesis, and qRT-PCR analyses were performed as in Figure 3. Plants were grown at 21°C under 24-h of light.

353

354 **DISCUSSION**

355

356 Here we present several lines of evidence in support of a direct interaction between the soluble N-
357 terminus and the soluble C-terminus of the plant mechanosensitive ion channel *At*MSL10. First, a
358 suite of temperature-sensitive phenotypes was produced by overexpression of *MSL10-GFP*, by
359 native expression of phospho-dead substitutions in MSL10's N-terminus, or by the S640L point
360 mutation in its C-terminus. Second, phospho-mimetic substitutions suppressed the effect of S640L
361 when both types of lesions were present in the same monomer. Third, the soluble N- and C-termini
362 of MSL10 interacted in two protein-protein interaction assays in a manner independent of
363 phospho-variant mutations or the S640L lesion. In addition, we showed that MSL10 activation
364 resulted in the upregulation of genes involved in a range of pathways that can be generally
365 characterized as responses to biotic and abiotic stress.

366

367 To date, functional characterization of MSL10 has been based on overexpression of *MSL10-GFP*
368 in *N. benthamiana* and Arabidopsis (Veley et al., 2014). Here, we show that two additional types
369 of *MSL10* gain-of-function lines (plants expressing endogenous levels of untagged *MSL10g*^{7A} or
370 harboring the *msl10-3G* allele) phenocopy *MSL10-GFP* overexpression lines, as does inducible
371 overexpression of MSL10^{7A} (**Figure 1**, **2, S2**, **S5**). Thus, the ability of MSL10 to induce growth
372 retardation, ectopic cell death, hyperaccumulation of H_2O_2, and the induction of genes related to
373 ROS, and cell death does not require overexpression or the presence of a tag, and therefore is likely
374 to be related to the normal function of MSL10. We note that plants overexpressing untagged wild
375 type *MSL10* do not show these phenotypes (Zou et al., 2015). Perhaps, in this context, a large tag
376 improves MSL10 stability.

377

378 Furthermore, the phenotypes associated with these *MSL10* gain-of-function lines was alleviated
379 by growth at elevated temperature, while protein abundance and localization at the cell periphery
380 remained unchanged (**Figure 3, S4** and **S6**). There is a growing list of plant defense response
381 mutants which display partial or complete suppression of similar growth defects and ectopic cell
382 death when grown at high temperatures (Yang et al., 2007; Gao et al., 2009; Wang et al., 2011;
383 Wierzba and Tax, 2016), suggesting that a shared pathway leading to these phenotypes is

384 temperature sensitive. Alternatively, growth at high temperature could affect MSL10 activity due
385 to alterations in membrane fluidity (Fan and Evans, 2015).
386
387 MSL10 likely functions as a homo-oligomer similar to *Ec*MscS, a homoheptameric (Bass et al.,
388 2002; Sukharev, 2002). Thus, the interactions we observe between the N- and the C-terminus could
389 be between domains on the same monomer, or between domains on different monomers once they
390 are assembled into a channel. To distinguish between these two possibilities will require further
391 study. These interactions occur in the absence of the membrane spanning domains, at least in the
392 transient expression system used for BiFC (**Figure 5B**). Neither N-terminal phosphorylation status
393 nor the C-terminal lesion S640L had any impact on the self-association of MSL10 in either BiFC
394 or mbSUS assays, suggesting that this is a stable interaction and is not a regulated step in the
395 activation of MSL10 (**Figure 5**).
396
397 Based on these results, we propose a three-step model for MSL10 activation, illustrated in **Figure**
398 **7**. According to this model, phosphorylation of its N-terminal domain maintains MSL10 in its
399 inactive form (**Figure 7A**). When membrane tension is increased, the channel opens, first resulting
400 in a structural rearrangement at the C-terminus. Second, this conformational change is transduced
401 to the N-terminal domain. Third, the subsequent conformational change of the N-terminus results
402 in its dephosphorylation. The dephosphorylated N-terminal domain (depicted in red) is then
403 capable of triggering a cell death signaling cascade through an unknown mechanism.
404 Dephosphorylation could arise through conformational changes that directly (or indirectly through
405 accessory proteins like 14-3-3 proteins (Moeller et al., 2016) make the N-terminus more accessible
406 to cytosolic phosphatases or less accessible to kinases. Conformational changes that lead to altered
407 phosphorylation status has been previously shown to activate hormone-receptor complexes in
408 plants (Zhang et al., 2014; Farrell and Breeze, 2018; Wang et al., 2019).
409
410 In the case of *MSL10-GFP* overexpression (**Figure 7B**), we propose that the appropriate kinase is
411 not sufficient to maintain the N-terminus in its dephosphorylated and deactivated, form, leading to
412 constitutive activation of the cell death signaling pathway. Phospho-dead versions of MSL10
413 (MSL10g^{7A}) are constitutively active and do not require added tension; conversely, phospho-
414 mimetic version of MSL10 (MSL10g^{7D}) are maintained in an inactive state (**Figure 7C**). As for

415 plants harboring the *MSL10*^{S640L}*-GFP* transgene or the *msl10-3G* mutant (**Figure 7D**), the S640L
416 mutation may mimic the conformational change that occurs during opening of the channel,
417 bypassing the normal activation of signaling by membrane tension and leading to constitutive
418 activation. Alternatively, S640L may alter the tension sensitivity or conductivity of MSL10. This
419 effect, however, is blocked by the presence of N-terminal phospho-mimetic substitutions, as shown
420 in plants constitutively expressing *MSL10*^{7D,S640L}*-GFP*. Thus, this three-step model is sufficient to
421 explain the phenotypic and genetic interaction data documented above.
422
423 The results presented here also begin to address how the activation of MSL10 leads to phenotypic
424 consequences. Our transcriptomic analyses show that MSL10 activation promotes the expression
425 of genes previously seen to be involved in the response to osmotic stress, biotic stress and
426 wounding (**Figure 6D**). In fact, signaling networks originating from diverse abiotic, biotic, and
427 mechanical stresses are highly integrated and often culminate in a common set of responses
428 (Walley et al., 2007; Macqueen and Bergelson, 2016; Zhang et al., 2016). *MSL10-GFP*
429 overexpressing lines resemble a number of other mutant or transgenic lines associated with
430 constitutive induction of biotic and abiotic stress responses, including the gain-of-function mutant
431 *SUPPRESSOR OF npr1-1, CONSTITUTIVE 1 (snc1), CHILLING SENSITIVE 2 (chs2), LESION*
432 *SIMULATING DISEASE 1 (lsd1)* and plants overexpressing a *TIR-X* gene (Zhang et al., 2003b;
433 Huang et al., 2010a; Huang et al., 2010b; Kato et al., 2014). Both abiotic and biotic stressors such
434 as dehydration, flooding, or fungal penetration could induce physical alterations in the plasma
435 membrane that are subsequently perceived as lateral membrane tension.
436
437 In summary, our three-step model for MSL10 activation, which involves an intra- and/or
438 intermolecular interaction between the soluble N- and C- termini of MSL10, explains the
439 phenotypic similarity shared by plants overexpressing MSL10-GFP, expressing the *MSL10*^{7A}
440 transgene, or harboring the *msl10-3G* allele. Gene expression analyses provide evidence that
441 MSL10 may serves as a broad sensor of membrane perturbation that, when over-activated, leads
442 to cell death. These results begin to build the groundwork for future investigations into the
443 molecular mechanism by which the mechanosensitive ion channel MSL10 functions.
444

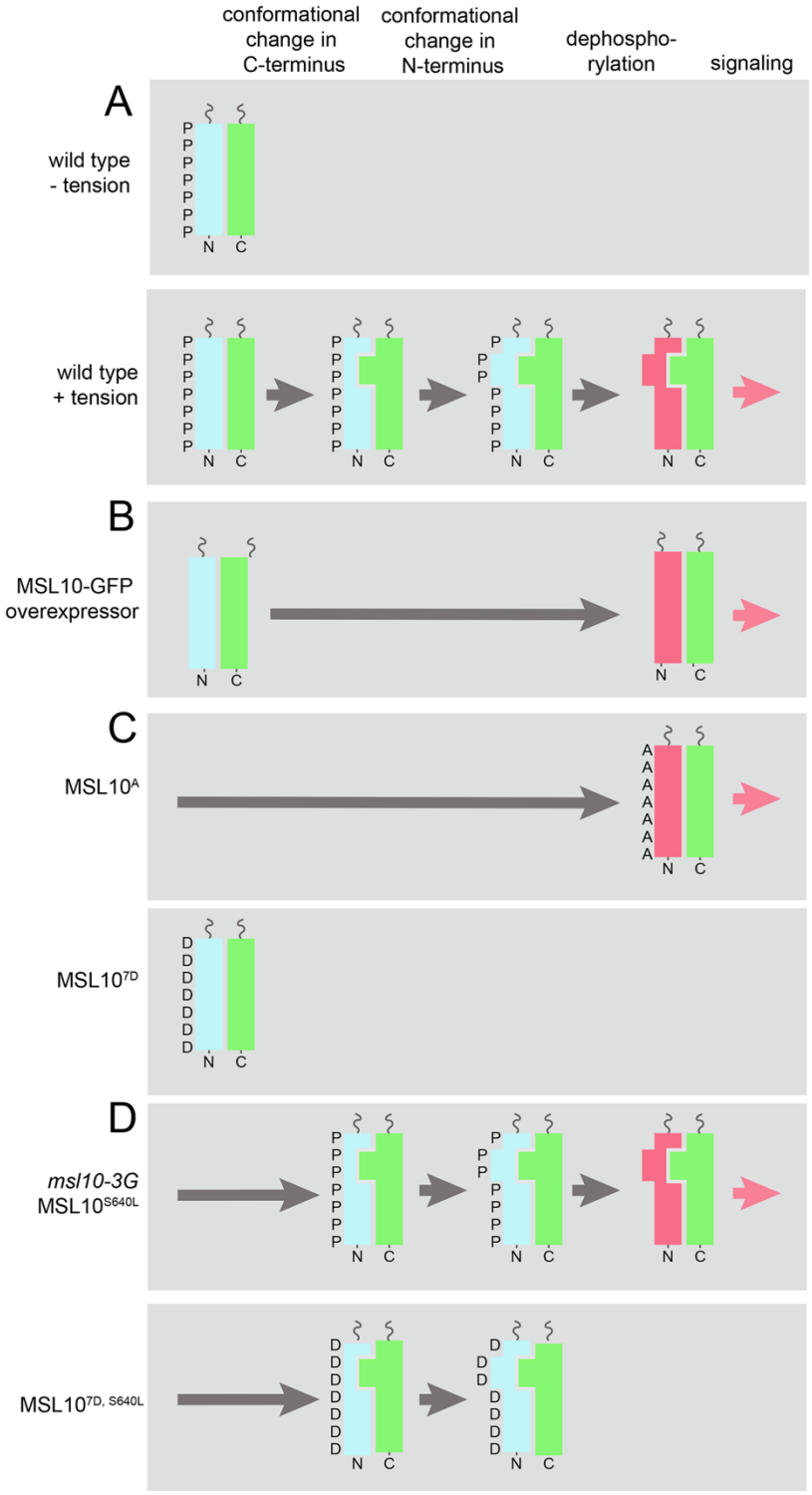

445

Figure 7. A three-step model for the regulation of MSL10's cell death signaling function

For simplicity, only the soluble N- and C-terminal domains of MSL10 are shown. They could be from the same or from different monomers. The inactive N-terminus, active N-terminus, and C-terminus are represented by rectangles colored blue, red, and green, respectively. Proposed conformational changes are indicated by changes in the shape of each rectangle. This model explains the signaling output (red arrow) observed in wild type plants (A), in response to MSL10-GFP overexpression (B), in the presence of MSL10 phospho-variants (C), in the presence of alleles or transgenes harboring the S640L mutation in the C-terminus (D, top), or in the presence of a transgene that combines S640L with phospho-mimetic substitutions in the N-terminus (D, bottom).

446 **METHODS**

447

448 **Sequence alignments**

449 The full-length amino acid sequence of *Arabidopsis thaliana* MSL10 was used as a BLASTp query
450 to search for homologs in selected plant species. The protein with the highest identity to *At*MSL10
451 in each species was chosen for the final alignment, using the PRALINE multiple sequence
452 alignment server (Bawono et al., 2017).

453

454 **Plant lines and growth conditions**

455 The plants used in this study are all in the Arabidopsis *Col-0* ecotype background. The T-DNA
456 insertion lines, including *msl10-1* (SALK_114626) and *msl9-1* (SALK_114361) was obtained
457 from the Arabidopsis Biological Resource Center (Haswell et al., 2008). The *rea1*/*msl10-3G*
458 mutant was obtained from the J.-M. Zhou lab (ShanghaiTech University, Shanghai). In most
459 experiments, plants were grown on soil at 21°C under a 24-h light regime (~120 μmol $m^{-2}s^{-1}$).
460 For experiments done at elevated temperature, plants were grown on soil at high temperature that
461 ranges from 28°C to 30°C under a 24-h light regime (~120 μmol $m^{-2}s^{-1}$). Backcrosses and
462 outcrosses were made through standard techniques and genotyped with PCR-based markers. The
463 *MSL10-GFP* overexpression lines are the same as those described in an earlier study (Veley et al.,
464 2014).

465

466 **Genotyping**

467 DNA was extracted by grinding tissue in extraction buffer (200 mM Tris-HCl pH 7.5, 250 mM
468 NaCl, 250 mM EDTA, 0.5% SDS) and precipitating with an equal volume of isopropanol. The
469 *msl10-3G*/*rea1* allele was genotyped by amplifying the genomic region surrounding the point
470 mutation using gene specific oligos listed in **Supplemental Table 5** followed by digestion with
471 *TaqI*α. restriction enzyme (NEB), which only digests the wild-type *MSL10* gene. PCR genotyping
472 of *msl10-1* and *msl9-1* alleles was performed as described (Haswell et al., 2008).

473

474 **Cloning and generation of transgenic plants**

475 $MSL10^{S640L}$ cDNA constructs were generated through site-directed mutagenesis as described
476 (Jensen and Haswell, 2012) using pENTRY clones (pENTR+*MSL10* and pENTR+$MSL10^{7D}$) as

477 template (Veley et al., 2014). They were cloned into pEarleyGate103 destination vectors (Earley
478 et al., 2006) using LR recombination. To construct *gMSL10* plasmids, the *MSL10* gene was
479 amplified from genomic wild-type *Col-0* DNA using gene-specific primers listed in **Table S5** and
480 cloned into pENTR/D-TOPO entry vector (Thermo Fisher Scientific), then recombined into
481 pBGW destination vectors (Karimi et al., 2002) by LR recombination. The $MSL10g^{7A}$ and
482 $MSL10g^{7D}$ constructs were generated in a single reaction using a two-fragment Gibson Assembly,
483 using Gibson Assembly NEB Mix and overlapping primers following manufacturer's
484 recommendation (Thermo Fisher Scientific). The assembled plasmids were then recombined into
485 pBGW destination vectors by LR recombination. All primers used for Gibson cloning are listed in
486 **Table S5**. For generating constructs for conditional expression of *MSL10* and its phospho-variants
487 ($MSL10^{4A}$ and $MSL10^{4D}$) under the dexamethasone (DEX)- inducible promoter, the Gateway
488 cassette-containing region from pEarleyGate100 (Earley et al., 2006), was amplified from the
489 plasmid introduced into the binary expression vector pTA7002 (Aoyama and Chua, 1997) using
490 XhoI and SpeI restriction sites. pENTR constructs containing coding region of *MSL10*, $MSL10^{4A}$
491 and $MSL10^{4D}$ (Veley et al., 2014) were used in recombination reactions with the pTA7002 vector
492 using LR clonase.
493
494 **Plant transformation**
495 All binary constructs were transformed into wild-type *Col-0, msl10-1* or *msl9-1; msl10-1* plants
496 with *Agrobacterium tumefaciens* GV3101 by floral dip (Clough and Bent, 1998). Homozygous T3
497 or T4 lines with a single transgene insertion were identified using selectable markers, PCR
498 genotyping, RT-PCR, and/or fluorescent GFP expression and immunodetection.
499
500 **Gene expression analysis**
501 Quantitative reverse-transcription polymerase chain reaction (qRT-PCR) was performed as
502 described (Hamilton et al., 2015) with minor modifications. Total RNA was isolated from the
503 rosette leaves of healthy 3-week-old plants (before yellow necrotic lesions develop) using the
504 RNeasy Plant Mini Kit (Qiagen). All results shown include data from three biological replicates;
505 for each biological replicate, three technical replicates were performed for each of three samples.
506 Transcript levels for each gene was normalized against the geometric mean of the threshold cycle
507 (ct) values of the two reference genes (Biazzi et al., 2015), namely *UBQ5* and *EF1α.* Finally,

508 relative abundance of transcripts was calculated using the $2^{-\Delta\Delta Ct}$ method (Livak and Schmittgen
509 2001). Semi-quantitative RT-PCR was performed as described (Veley et al., 2014). For **Figure**
510 **S3A**, 10 µM DEX (Sigma-Aldrich), dissolved in 0.016% ethanol, was infiltrated into 5-week-old
511 leaves. Tissue was harvested for RNA isolation 12 h post-infiltration. The primers used are listed
512 in **Table S5.**
513
514 **Immunodetection**
515 Total proteins were extracted from non-chlorotic leaves of three-week-old plants as described
516 (Veley et al. 2014). Proteins samples were resolved by 10% SDS-PAGE and transferred to
517 polyvinylidene difluoride membranes (Millipore) for 16 h at 100 mA. Transferred proteins were
518 probed with anti-tubulin (Sigma, 1:10,000 dilution) and anti-GFP (Takara Bio, 1:5,000 dilution)
519 antibodies with incubation for 1 h and 16 h, respectively. After incubation for 1 h with horseradish
520 peroxidase-conjugated anti-mouse secondary antibodies (1:10,000 dilution; Millipore). Detection
521 was performed using the SuperSignal West Dura Detection Kit (Thermo Fisher Scientific).
522
523 **Statistical analyses**
524 Statistical evaluations were conducted using R Studio software (RStudio). Statistical differences
525 were analyzed as indicated in the figure legends.
526
527 **Trypan blue staining and quantification**
528 Cell death was visualized in leaves of three to four-week-old soil-grown plants using Trypan blue
529 staining as described (Veley et al., 2014). Images were obtained with an Olympus DP80 equipped
530 with a cooled color digital camera. The size of Trypan blue stained regions was quantified using
531 ImageJ software as described (Fernández-Bautista et al., 2016).
532
533 **Detection and quantification of reactive oxygen species**
534 Superoxide anion radical accumulation was detected by NitroBlue Tetrazolium chloride (NBT;
535 Sigma) as described previously (Wilson et al., 2016). The amount of formazan was determined by
536 measuring lysates at an absorbance of 700 nm using a 96-well microplate reader (Infinite 200 PRO;
537 Tecan). Absorbance reads were normalized to the fresh weight of the leaves. H_2O_2 levels were
538 measured by 3,3′-diaminobenzidine (DAB, Sigma) staining (Veley et al., 2014). For the

539 quantitative measurement of hydrogen peroxide concentrations, the Amplex Red
540 Hydrogen/Peroxidase Assay Kit (Molecular Probes, Invitrogen) was used, following the
541 manufacturer's instructions and as described in (Wilson et al., 2016).
542
543 **Transcriptomic analysis by RNA sequencing**
544 Wild type and the *MSL10-GFP* overexpressing line, *12-3* were grown for three-weeks at 21°C
545 under 24h light regime (~120 µmol $m^{-2}s^{-1}$), then half of the plants were transferred to 30°C for
546 24 hours. RNA was extracted from the entire rosette tissue of three-week-old plants using the Plant
547 RNeasy Kit following manufacturer's instructions. The RNA samples were outsourced to Cofactor
548 Genomics (St. Louis, MO) for poly-A purification, library construction, sequencing and
549 preliminary analysis. Illumina TruSeq unstranded mRNA libraries were prepared and sequenced
550 on an Illumina HiSeq2500 with single end 50nt reads. Raw data for each library was assessed
551 using FASTQC, which revealed no adaptor contamination. The raw data were aligned directly to
552 the Araport11 cDNA annotations using kallisto v0.44.0 (Bray et al., 2016). Raw counts were used
553 as input for edgeR v3.18.1 (Robinson et al., 2010), normalized to library size, and initially filtered
554 to retain all cDNAs with at least 1 count per million mapped reads (cpm) in at least two libraries.
555 A multidimensional scaling (MDS) plot was constructed with the plotMDS() function (Smyth,
556 2005). Library cpm counts were scaled, k-means clustered with the kmeans function in R and
557 centroids were visually inspected for upregulation in the "MSL10 O/E 21°C" condition. To
558 identify genes with increased pseudocounts in the "MSL10 O/E 21°C" condition relative to all
559 other libraries, cDNAs were annotated for function using ThaleMine v1.10.4 (Krishnakumar et al.,
560 2017). For GO enrichment analysis, differentially expressed nonredundant genes (N = 5828) were
561 assessed using PANTHER version 14.0 (Mi et al., 2017). A statistical overrepresentation test using
562 default settings ($P < 0.0001$, Bonferroni correction) was used to determine overrepresented GO
563 terms for the PANTHER biological process data set.
564
565 **Split-Ubiquitin Yeast two hybrid assay (mbSUS)**
566 Intramolecular interaction between MSL10 N- and C-termini was determined using the mating-
567 based split-ubiquitin system as described (Obrdlik et al., 2004; Lee et al., 2019). Strength of
568 interaction is quantified by CPRG, a chlorophenol red-β-D-galactopyranoside colorimetric
569 reporter (Bhaskara et al., 2012). The PCR primers used for creating constructs for mbSUS assay

570 are listed in **Table S5.** All the yeast vectors were obtained from Arabidopsis Biological Resource
571 Center.
572
573 **Bimolecular Fluorescence Complementation (BiFC) assays**
574 Entry vectors containing various truncated versions of MSL10 coding region were recombined
575 into the binary vector pDEST-VYCE(R)GW or pDEST-VYNE(R)GW (Gehl et al., 2009), which
576 carry the C-terminal or N-terminal fragment of Venus YFP, respectively, using LR Clonase. The
577 PCR primers used for BiFC assay are listed in **Table S5**. All the BiFC fusion proteins were tagged
578 at the C-terminus. The plasmids were introduced into *Agrobacterium strain GV3101* and pairwise
579 combinations were co-infiltrated into 4- to 6-week-old *N. benthamiana* leaves as described (Waadt
580 and Kudla, 2008). To suppress posttranscriptional gene silencing, each construct pair was co-
581 infiltrated with *Agrobacterium* strain *AGL-1* harboring p19 (Voinnet et al., 2002). Infiltrated
582 abaxial leaf areas were examined for YFP signal using a confocal microscope (Olympus Fluoview
583 FV 3000) at 3 to 5 d post-inoculation. The experiments were performed at least three times using
584 different batches of plants; for each biological replicate, three independent *N. benthamiana* plants
585 were infiltrated. The microscope and camera settings used were as described (Veley et al., 2014).
586
587 **Accession numbers**
588 GenBank accession numbers used in **Figure 1** are: *Arabidopsis thaliana* (NP_196769.1),
589 *Arabidopsis lyrata* (XP_002873549.1), *Brassica rapa* (XP_009121883.1), *Brassica napus*
590 (XP_013676093.1), *Camelina sativa* (XP_010453270.1), *Populus trichocarpa*
591 (POPTR_0006s14640g), *Medicago truncatula* (XP_003603202.2), *Vitis vinefera*
592 (XP_002279755.1), *Solanum lycopersicum* (XP_004245056.1), *Solanum tuberosum*
593 (XP_006350354.1), *Zea mays* (XP_008649202.1), *Oryza sativa* (XP_015641284.1), *Sorghum*
594 *bicolor* (XP_002438025.1), *Brachypodium distachyon* (XP_003560953.1), *Setaria italica*
595 (XP_004964936.1).
596
597 The rest of the genes referred to in this study correspond to the following Arabidopsis Genome
598 Initiative locus identifiers: *MSL9 (At5G19520), MSL10 (At5G12080), RAP2.6 (At1g43160), AOS*
599 *(At5g42650), LOX2 (At3g45140), PDF1.2 (At5G44420), SAG12 (At3g20770), PERX34*
600 *(At3g49120), DOX1 (At3g01420), OSM34 (At4G11650), UBQ5 (At3g62250), EF1α (At5g60390),*

601 *SAG13 (At2g29350), LOX3 (At1g17420), ELI3-2 (At4g37990). PP2C-1 (At5g59220), TBL8*
602 *(At3g11480).*
603
604 **AUTHOR CONTRIBUTIONS**
605
606 D.B. and E.S.H. conceived the project and designed the experiments. A.H. performed the RNA-
607 seq analysis and contributed data to Figures 6B, S8, Table S1 and Table S2; J.M.S. contributed
608 data to Figures 1C, 3C, and 4; K.M.V. contributed data to Figure 3A and Figure S4A; E.S.H.
609 contributed data to Figure 1B and conceived the model in Figure 7. D.B. performed the rest of the
610 experiments. D.B., and E.S.H. wrote the manuscript with input from J.M.S., A.H. and K.M.V.
611
612 **ACKNOWLEDGMENTS**
613
614 We thank J.-M. Zhou (ShanghaiTech University, Shanghai) for providing *rea1* mutant seeds and
615 the Arabidopsis Biological Resource Center for seeds and for vectors used in BiFC and mbSUS
616 assays. We also are grateful to Ivan Radin, Yanbing Wang, Kari Miller and Angela Schlegel for
617 critical reading of the manuscript. This work was supported by NSF MCB-1253103 and the NSF
618 Center for Engineering Mechanobiology Award 1548571. J.M.S. was supported by NSF Graduate
619 Research Fellowship DGE-1745038. A.H was supported by an NSF National Plant Genome
620 Initiative Postdoctoral Research Fellowship in Biology Award 1611853. No conflicts of interest
621 declared.
622
623 **REFERENCES**
624 **Aoyama, T., and Chua, N.** (1997). A glucocorticoid-mediated transcriptional induction system
625 in transgenic plants. *Plant Journal* **11**:605–612.
626 **Bass, R. B., Strop, P., Barclay, M., and Rees, D. C.** (2002). Crystal structure of *Escherichia*
627 *coli* MscS, a voltage-modulated and mechanosensitive channel. *Science* **298**:1582–1587.
628 **Basu, D., and Haswell, E. S.** (2017). Plant mechanosensitive ion channels: an ocean of
629 possibilities. *Current Opinion in Plant Biology* **40**:43–48.
630 **Bavi, N., Nikolaev, Y. A., Bavi, O., Ridone, P., Martinac, A. D., Nakayama, Y., Cox, C. D.,**
631 **and Martinac, B.** (2017). Principles of mechanosensing at the membrane interface. In *The*

632 *Biophysics of Cell Membranes: Biological Consequences* (ed. Epand, R. M. and
633 Ruysschaert, J.-M.), pp. 85–119. Singapore: Springer Singapore.
634 **Bawono, P., Dijkstra, M., Pirovano, W., Feenstra, A., Abeln, S., and Heringa, J.** (2017).
635 Multiple sequence alignment. In *Bioinformatics: Volume I: Data, Sequence Analysis, and*
636 *Evolution* (ed. Keith, J. M.), pp. 167–189. New York, NY: Springer New York.
637 **Bhaskara, G. B., Nguyen, T. T., and Verslues, P. E.** (2012). Unique drought resistance
638 functions of the highly ABA-induced clade A protein phosphatase 2Cs. *Plant Physiology*
639 **160**:379–395.
640 **Biazzi, E., Carelli, M., Tava, A., Abbruscato, P., Losini, I., Avato, P., Scotti, C., and**
641 **Calderini, O.** (2015). CYP72A67 catalyzes a key oxidative step in *Medicago truncatula*
642 hemolytic saponin biosynthesis. *Molecular Plant* **8**:1493–1506.
643 **Bray, N. L., Pimentel, H., Melsted, P., and Pachter, L.** (2016). Near-optimal probabilistic
644 RNA-seq quantification. *Nature Biotechnology* **34**:525–527.
645 **Clough, S. J., and Bent, A. F.** (1998). Floral dip: a simplified method for Agrobacterium -
646 mediated transformation of *Arabidopsis thaliana*. *The Plant Journal* **16**:735–743.
647 **Earley, K. W., Haag, J. R., Pontes, O., Opper, K., Juehne, T., Song, K., and Pikaard, C. S.**
648 (2006). Gateway-compatible vectors for plant functional genomics and proteomics. *Plant*
649 *Journal* **45**:616–629.
650 **Fan, W., and Evans, R. M.** (2015). Turning up the heat on membrane fluidity. *Cell* **161**:962–
651 963.
652 **Farrell, B., and Breeze, A. L.** (2018). Structure, activation and dysregulation of fibroblast
653 growth factor receptor kinases: perspectives for clinical targeting. *Biochemical Society*
654 *Transactions* **46**:1753–1770.
655 **Fernández-Bautista, N., Domínguez-Núñez, J. A., Moreno, M. M. C., and Berrocal-Lobo,**
656 **M.** (2016). Plant tissue trypan blue staining during phytopathogen infection. *Bio-protocol*
657 **6**:e2078.
658 **Gao, M., Wang, X., Wang, D., Xu, F., Ding, X., Zhang, Z., Bi, D., Cheng, Y. T., Chen, S.,**
659 **Li, X., et al.** (2009). Regulation of cell death and innate immunity by two receptor-like
660 kinases in Arabidopsis. *Cell Host and Microbe* **6**:34–44.
661 **Gehl, C., Waadt, R., Mendel, R., and Ha, R.** (2009). New GATEWAY vectors for high-
662 throughput analyses of protein – protein interactions by bimolecular fluorescence

663 complementation. *Molecular Plant* **2**:1051–1058.
664 **Gobert, A., Isayenkov, S., Voelker, C., Czempinski, K., and Maathuis, F. J. M.** (2007). The
665 two-pore channel *TPK1* gene encodes the vacuolar K^+ conductance and plays a role in K^+
666 homeostasis. *Proceedings of the National Academy of Sciences of the United States of*
667 *America* **104**:1–6.
668 **Gray, W. M., Ostin, A., Sandberg, G., Romano, C. P., and Estelle, M.** (1998). High
669 temperature promotes auxin-mediated hypocotyl elongation in Arabidopsis. *Proceedings of*
670 *the National Academy of Sciences of the United States of America* **95**:7197–7202.
671 **Hamant, O., and Haswell, E. S.** (2017). Life behind the wall: sensing mechanical cues in
672 plants. *BMC Biology* **15**:59.
673 **Hamilton, E. S., Jensen, G. S., Maksaev, G., Katims, A., Sherp, A. M., and Haswell, E. S.**
674 (2015). Mechanosensitive channel MSL8 regulates osmotic forces during pollen hydration
675 and germination. *Science* **350**:438–441.
676 **Haswell, E. S., and Meyerowitz, E. M.** (2006). MscS-like proteins control plastid size and
677 shape in *Arabidopsis thaliana*. *Current Biology* **16**:1–11.
678 **Haswell, E. S., Peyronnet, R., Barbier-Brygoo, H., Meyerowitz, E. M., and Frachisse, J. M.**
679 (2008). Two MscS homologs provide mechanosensitive channel activities in the
680 Arabidopsis root. *Current Biology* **18**:730–734.
681 **Hou, C., Tian, W., Kleist, T., He, K., Garcia, V., Bai, F., Hao, Y., Luan, S., and Li, L.**
682 (2014). Osmosensitive calcium-permeable cation channels 632 DUF221 proteins are a
683 family of osmosensitive calcium- permeable cation channels conserved across eukaryotes.
684 *Cell Research* **24**:632–635.
685 **Huang, X., Li, Y., Zhang, X., Zuo, J., and Yang, S.** (2010a). The Arabidopsis LSD1 gene
686 plays an important role in the regulation of low. *New Phytologist* **187**:301–12.
687 **Huang, X., Li, J., Bao, F., Zhang, X., and Yang, S.** (2010b). A gain-of-function mutation in
688 the Arabidopsis disease resistance gene *RPP4* confers sensitivity to low temperature. *Plant*
689 *Physiology* **154**:796–809.
690 **Ichimura, K., Casais, C., Peck, S. C., Shinozaki, K., and Shirasu, K.** (2006). MEKK1 is
691 required for MPK4 activation and regulates tissue-specific and temperature-dependent cell
692 death in Arabidopsis. *Journal of Biological Chemistry* **281**:36969–36976.
693 **Jayaraman, D., Gilroy, S., and Ané, J. M.** (2014). Staying in touch: Mechanical signals in

694 plant-microbe interactions. *Current Opinion in Plant Biology* **20**:104–109.
695 **Jensen, G. S., and Haswell, E. S.** (2012). Functional analysis of conserved motifs in the
696 mechanosensitive channel homolog MscS-Like2 from *Arabidopsis thaliana*. *PLoS ONE* **7**.
697 **Karimi, M., Inzé, D., and Depicker, A.** (2002). GATEWAY^{TM} vectors for Agrobacterium-
698 mediated plant transformation. *Trends in Plant Science* **7**:193–195.
699 **Kato, H., Saito, T., Ito, H., Komeda, Y., and Kato, A.** (2014). Overexpression of the *TIR-X*
700 gene results in a dwarf phenotype and activation of defense-related gene expression in
701 *Arabidopsis thaliana*. *Journal of Plant Physiology* **171**:382–388.
702 **Kierzkowski, D.** (2019). Cellular basis of growth in plants : geometry matters. *Current Opinion*
703 *in Plant Biology* **47**:56–63.
704 **Koini, M. A., Alvey, L., Allen, T., Tilley, C. A., Harberd, N. P., Whitelam, G. C., and**
705 **Franklin, K. A.** (2009). High temperature-mediated adaptations in plant architecture
706 require the bHLH transcription factor PIF4. *Current Biology* **19**:408–413.
707 **Kovalchuk, N., Jia, W., Eini, O., Morran, S., Pyvovarenko, T., Fletcher, S., Bazanova, N.,**
708 **Harris, J., Beck-Oldach, K., Shavrukov, Y., et al.** (2013). Optimization of TaDREB3
709 gene expression in transgenic barley using cold-inducible promoters. *Plant Biotechnology*
710 *Journal* **11**:659–670.
711 **Krishnakumar, V., Contrino, S., Cheng, C. Y., Belyaeva, I., Ferlanti, E. S., Miller, J. R.,**
712 **Vaughn, M. W., Micklem, G., Town, C. D., and Chan, A. P.** (2017). Thalemine: A
713 warehouse for Arabidopsis data integration and discovery. *Plant and Cell Physiology* **58**:e4.
714 **Lee, C. P., Maksaev, G., Jensen, G. S., Murcha, M. W., Wilson, M. E., Fricker, M., Hell, R.,**
715 **Haswell, E. S., Millar, A. H., and Sweetlove, L. J.** (2016). MSL1 is a mechanosensitive
716 ion channel that dissipates mitochondrial membrane potential and maintains redox
717 homeostasis in mitochondria during abiotic stress. *Plant Journal* **88**:809–825.
718 **Lee, J. S., Wilson, M. E., Richardson, R. A., and Haswell, E. S.** (2019). Genetic and physical
719 interactions between the organellar mechanosensitive ion channel homologs MSL1, MSL2,
720 and MSL3 reveal a role for inter-organellar communication in plant development. *Plant*
721 *Direct* **3**:e00124.
722 **Livak, K. J., and Schmittgen, T. D.** (2001). Analysis of relative gene expression data using
723 real-time quantitative PCR and the 2-ΔΔCT method. *Methods* **25**:402–408.
724 **Maathuis, F. J. M.** (2011). Vacuolar two-pore K^+ channels act as vacuolar osmosensors. *New*

725 *Phytologist* **191**:84–91.
726 **Machiyama, H., Tatsumi, H., and Sokabe, M.** (2009). Structural changes in thecytoplasmic
727 domain of the mechanosensitive channel MscS during opening. *Biophysical Journal*
728 **97**:1048–1057.
729 **Macqueen, A., and Bergelson, J.** (2016). Modulation of R-gene expression across
730 environments. *Journal of Experimental Botany* **67**:2093–2105.
731 **Maksaev, G., and Haswell, E. S.** (2012). MscS-Like10 is a stretch-activated ion channel from
732 Arabidopsis thaliana with a preference for anions. *Proceedings of the National Academy of*
733 *Sciences of the United States of America* **109**:19015–20.
734 **Maksaev, G., Shoots, J. M., Ohri, S., and Haswell, E. S.** (2018). Nonpolar residues in the
735 presumptive pore-lining helix of mechanosensitive channel MSL10 influence channel
736 behavior and establish a nonconducting function. *Plant Direct* **2**:e00059.
737 **Martinac, B., Nomura, T., Chi, G., Petrov, E., Rohde, P. R., Battle, A. R., Foo, A.,**
738 **Constantine, M., Rothnagel, R., Carne, S., et al.** (2013). Bacterial mechanosensitive
739 channels: Models for studying mechanosensory transduction. *Antioxidants & Redox*
740 *Signaling* **20**:952–969.
741 **Mi, H., Huang, X., Muruganujan, A., Tang, H., Mills, C., Kang, D., and Thomas, P. D.**
742 (2017). PANTHER version 11: Expanded annotation data from Gene Ontology and
743 Reactome pathways, and data analysis tool enhancements. *Nucleic Acids Research*
744 **45**:D183–D189.
745 **Moeller, H. B., Slengerik-Hansen, J., Aroankins, T., Assentoft, M., MacAulay, N.,**
746 **Moestrup, S. K., Bhalla, V., and Fenton, R. A.** (2016). Regulation of the water channel
747 aquaporin-2 via 14-3-3θ and -ζ. *Journal of Biological Chemistry* **291**:2469–2484.
748 **Monshausen, G. B., and Haswell, E. S.** (2013). A force of nature: Molecular mechanisms of
749 mechanoperception in plants. *Journal of Experimental Botany* **64**:4663–4680.
750 **Mori, K., Renhu, N., Naito, M., Nakamura, A., Shiba, H., Yamamoto, T., Suzaki, T., Iida,**
751 **H., and Miura, K.** (2018). Ca^{2+}-permeable mechanosensitive channels MCA1 and MCA2
752 mediate cold-induced cytosolic Ca^{2+} increase and cold tolerance in Arabidopsis. *Scientific*
753 *reports* **8**:550.
754 **Murthy, S. E., Dubin, A. E., Whitwam, T., Jojoa-Cruz, S., Cahalan, S. M., Mousavi, S. A.**
755 **R., Ward, A. B., and Patapoutian, A.** (2018). OSCA/TMEM63 are an evolutionarily

756 conserved family of mechanically activated ion channels. *eLife* **7**:e41844.
757 **Nakagawa, Y., Katagiri, T., Shinozaki, K., Qi, Z., Tatsumi, H., Furuichi, T., Kishigami, A.,**
758 **Sokabe, M., Kojima, I., Sato, S., et al.** (2007). Arabidopsis plasma membrane protein
759 crucial for Ca^{2+} influx and touch sensing in roots. *Proceedings of the National Academy of*
760 *Sciences of the United States of America* **104**:3639–3644.
761 **Obrdlik, P., El-Bakkoury, M., Hamacher, T., Cappellaro, C., Vilarino, C., Fleischer, C.,**
762 **Ellerbrok, H., Kamuzinzi, R., Ledent, V., Blaudez, D., et al.** (2004). K^+ channel
763 interactions detected by a genetic system optimized for systematic studies of membrane
764 protein interactions. *Proceedings of the National Academy of Sciences of the United States*
765 *of America* **101**:12242–12247.
766 **Pivetti, C. D., Yen, M.-R., Miller, S., Busch, W., Tseng, Y.-H., Booth, I. R., and Saier Jr,**
767 **M. H.** (2003). Two families of mechanosensitive channel proteins. *Microbiology and*
768 *Molecular Biology Reviews* **67**:66–85.
769 **Quint, M., Barkawi, L. S., Fan, K.-T., Cohen, J. D., and Gray, W. M.** (2009). Arabidopsis
770 IAR4 modulates auxin response by regulating auxin homeostasis. *Plant Physiology*
771 **150**:748–758.
772 **Ranade, S. S., Syeda, R., and Patapoutian, A.** (2015). Mechanically activated ion channels.
773 *Neuron* **87**:1162–1179.
774 **Reinders, A., Schulze, W., Thaminy, S., Stagljar, I., Frommer, W. B., and Ward, J. M.**
775 (2002). Intra- and intermolecular interactions in sucrose transporters at the plasma
776 membrane detected by the split-ubiquitin system and functional assays. *Structure* **10**:763–
777 772.
778 **Robinson, M. D., McCarthy, D. J., and Smyth, G. K.** (2010). edgeR: a Bioconductor package
779 for differential expression analysis of digital gene expression data. *Bioinformatics (Oxford,*
780 *England)* **26**:139–140.
781 **Rowe, I., Anishkin, A., Kamaraju, K., Yoshimura, K., and Sukharev, S.** (2014). The
782 cytoplasmic cage domain of the mechanosensitive channel MscS is a sensor of
783 macromolecular crowding. *The Journal of General Physiology* **143**:543–557.
784 **Smyth, G. K.** (2005). Linear models for microarray data. In *Bioinformatics and Computational*
785 *Biology Solutions Using R and Bioconductor* (ed. Gentleman, R.), Carey, V. J., Huber, W.,
786 Irizarry, R. A., and Dudoit, S., pp. 397–420. New York, NY: Springer New York.

787 **Spartz, A. K., Lee, S. H., Wenger, J. P., Gonzalez, N., Itoh, H., Inzé, D., Peer, W. A.,**
788 **Murphy, A. S., Overvoorde, P. J., and Gray, W. M.** (2012). The SAUR19 subfamily of
789 *SMALL AUXIN UP RNA* genes promote cell expansion. *The Plant Journal* **70**:978–990.
790 **Sukharev, S.** (2002). Purification of the small mechanosensitive channel of *Escherichia coli*
791 (MscS): the subunit structure, conduction, and gating characteristics in liposomes.
792 *Biophysical Journal* **83**:290–298.
793 **Veley, K. M., Marshburn, S., Clure, C. E., and Haswell, E. S.** (2012). Mechanosensitive
794 channels protect plastids from hypoosmotic stress during normal plant growth. *Current*
795 *Biology* **22**:408–413.
796 **Veley, K. M., Maksaev, G., Frick, E. M., January, E., Kloepper, S. C., and Haswell, E. S.**
797 (2014). *Arabidopsis* MSL10 has a regulated cell death signaling activity that is separable
798 from its mechanosensitive ion channel activity. *The Plant Cell* **26**:3115–3131.
799 **Voinnet, O., Pinto, Y. M., and Baulcombe, D. C.** (2002). Suppression of gene silencing: A
800 general strategy used by diverse DNA and RNA viruses of plants. *Proceedings of the*
801 *National Academy of Sciences* **96**:14147–14152.
802 **Waadt, R., and Kudla, J.** (2008). In plant visualization of protein interactions using
803 bimolecular fluorescence complementation (BiFC). *Cold Spring Harbor Protocols* **3**:1–8.
804 **Walley, J. W., Coughlan, S., Hudson, M. E., Covington, M. F., Kaspi, R., Banu, G.,**
805 **Harmer, S. L., and Dehesh, K.** (2007). Mechanical stress induces biotic and abiotic stress
806 responses via a novel cis-element. *PLoS Genetics* **3**:1800–1812.
807 **Wang, W., Dong, C., Naismith, J. H., Black, S. S., Edwards, M. D., Miller, S., Morrison, E.**
808 **L., Bartlett, W., and Booth, I. R.** (2008). The structure of an open form of an *E. coli*
809 mechanosensitive channel at 3.45 å resolution. *Science* **321**:1179–1183.
810 **Wang, Z., Meng, P., Zhang, X., Ren, D., and Yang, S.** (2011). BON1 interacts with the protein
811 kinases BIR1 and BAK1 in modulation of temperature-dependent plant growth and cell
812 death in Arabidopsis. *Plant Journal* **67**:1081–1093.
813 **Wang, J., Wang, J., Hu, M., Wu, S., Qi, J., Wang, G., Han, Z., Qi, Y., Gao, N., Wang, H.-**
814 **W., et al.** (2019). Ligand-triggered allosteric ADP release primes a plant NLR complex.
815 *Science* **364**:eaav5868.
816 **Wierzba, M. P., and Tax, F. E.** (2016). An allelic series of *bak1* mutations differentially alter
817 bir1 cell death, immune response, growth, and root development phenotypes in *Arabidopsis*

818 *thaliana*. *Genetics* **202**:689–702.
819 **Wilson, M. E., Mixdorf, M., Berg, R. H., and Haswell, E. S.** (2016). Plastid osmotic stress
820 influences cell differentiation at the plant shoot apex. *Development* **143**:3382–3393.
821 **Yang, H., Yang, S., Li, Y., and Hua, J.** (2007). The Arabidopsis BAP1 and BAP2 genes are
822 general inhibitors of programmed cell death. *Plant Physiology* **145**:135–146.
823 **Yuan, F., Yang, H., Xue, Y., Kong, D., Ye, R., Li, C., Zhang, J., Theprungsirikul, L., Shrift,**
824 **T., Krichilsky, B., et al.** (2014). OSCA1 mediates osmotic-stress-evoked Ca^{2+} increases
825 vital for osmosensing in Arabidopsis. *Nature* **514**:367–71.
826 **Zhang, X., Liang, R., Chen, X., Yang, F., and Zhang, L.** (2003a). Transgene inheritance and
827 quality improvement by expressing novel HMW glutenin subunit (HMW-GS) genes in
828 winter wheat. *Chinese Science Bulletin* **48**:771–776.
829 **Zhang, Y., Goritschnig, S., Dong, X., and Li, X.** (2003b). A gain-of-function mutation in a
830 plant disease resistance gene leads to constitutive activation of downstream signal
831 transduction pathways in *suppressor of npr1-1, constitutive 1*. *The Plant Cell* **15**:2636–
832 2646.
833 **Zhang, J., Yu, J., and Wen, C.-K.** (2014). An alternate route of ethylene receptor signaling.
834 *Frontiers in Plant Science* **5**:1–6.
835 **Zhang, M., Koh, J., Liu, L., Shao, Z., Liu, H., Hu, S., Zhu, N., Dufresne, C. P., Chen, S.,**
836 **and Wang, Q.** (2016). Critical role of COI1-dependent jasmonate pathway in AAL toxin-
837 induced PCD in tomato revealed by comparative proteomics. *Scientific Reports* **6**:1–14.
838 **Zhang, Z., Tateda, C., Jiang, S., Shrestha, J., Jelenska, J., Speed, D. J., and Greenberg, J.**
839 **T.** (2017). A suite of receptor-like kinases and a putative mechano-sensitive channel are
840 involved in autoimmunity and plasma membrane – based defenses in Arabidopsis.
841 *Molecular Plant-Microbe Interactions* **30**:150–160.
842 **Zhang, Z., Tong, X., Liu, S.-Y., Chai, L.-X., Zhu, F.-F., Zhang, X.-P., Zou, J.-Z., and Wang,**
843 **X.-B.** (2019). Genetic analysis of a Piezo-like protein suppressing systemic movement of
844 plant viruses in *Arabidopsis thaliana*. *Scientific Reports* **9**:3187.
845 **Zou, Y., Chintamanani, S., He, P., Fukushige, H., Yu, L., Shao, M., Zhu, L., Hildebrand, D.**
846 **F., Tang, X., and Zhou, J.-M.** (2015). A gain-of-function mutation in Msl10 triggers cell
847 death and wound-induced hyperaccumulation of JA in Arabidopsis. *Journal of Integrative*
848 *Plant Biology* **58**:600–609.

849

850 **Figure 1. *MSL10-GFP* overexpression lines, *msl10-3G* mutants, and *MSL10g^{7A}* lines have**
851 **similar whole-plant phenotypes. (A)** Predicted topology of an *At*MSL10 monomer. Teal,
852 cytosolic N-terminus; yellow, transmembrane helices; green, cytosolic C-terminus. Black triangles
853 denote the positions of the residues mutated in this study. The MscS domain is as defined in (Veley
854 et al. 2014). **(B)** Multiple alignment of protein sequences corresponding to the N-terminus of
855 putative *At*MSL10 orthologs in the *Brassicaceae* family. Darker teal shading indicates higher
856 conservation score and identical amino acids with an asterisk. **(C)** Multiple alignment of protein
857 sequences corresponding to the C-terminus of putative *At*MSL10 orthologs in selected flowering
858 plants. Conservation of residues is indicated as in **(B). (D)** and **(E)** T4 homozygous lines
859 overexpressing *MSL10-GFP* in the *Col-0* background (line *15-2*), T3 homozygous lines expressing
860 *MSL10g*, or *MSL10g^{7D}* in the *msl10-1* background, and T3 segregating or T3 homozygous lines
861 expressing *MSL10g^{7A}* in the *msl10-1* background were selected for comparison. **(D)** Whole-plant
862 images of 25-day-old plants of the indicated genotypes grown side-by-side at 21°C under a 24-h
863 light regime. Bar = 0.5 cm. **(E)** Petiole length of the fourth or fifth leaf from 28-day-old plants.
864 Different letters indicate significant differences as determined by one-way ANOVA followed by
865 Tukey's post-hoc test ($P < 0.05$). Error bars indicate ± SD of three replicates (n = 18 per replicate).
866

867 **Figure 2. *MSL10-GFP* overexpression lines, *msl10-3G* mutants, and *MSL10g^{7A}* lines display**
868 **similar expression profiles.** Quantitative RT-PCR analysis of four genes previously shown to be
869 upregulated in *35S:MSL10-GFP* overexpression lines **(A)** and four genes previously shown to be
870 upregulated in the *msl10-3G* allele **(B)**. cDNA was synthesized from total RNA extracted from
871 rosette leaves of three-week-old plants grown at 21°C under 24 hours of light. Expression levels
872 of respective genes were normalized to both *EF1α* and *UBQ5*. Mean fold-change values relative
873 to the wild type are plotted, with error bars showing ± SE of the mean of three biological replicates
874 Different letters indicate significant difference as determined by one-way ANOVA followed by
875 Tukey's post-hoc test ($P < 0.05$). For transgenics, two independent T3 or T4 homozygous lines
876 were selected for comparison.
877

878 **Figure 3. Growth at high temperatures suppresses phenotypes associated with *MSL10-GFP***
879 **overexpression.** Wild type, *msl10-1*, and three independent T4 homozygous lines expressing

880 *35S:MSL10-GFP* in the Col-0 background were grown side-by-side on soil under 24 h light regime
881 and at either 21°C or 28°-30°C. **(A)** Images of whole three-week-old plants. Bar = 0.5 cm. **(B)**
882 Relative transcript abundance of *MSL10* analyzed by with qRT-PCR from wild type, *msl10-1*, and
883 *35S:MSL10-GFP* line *15-2*. Inset compares *MSL10* expression levels in wild-type and *msl10-1*
884 lines only. **(C)** Immunoblot analysis of MSL10-GFP levels in rosette leaves of two-week old
885 plants. MSL10-GFP was detected with an anti-GFP primary antibody (top), and then the blot was
886 stripped and re-probed with an anti-α-tubulin primary antibody (bottom). Expected protein sizes
887 are indicated at the left according to a commercially available standard. **(D)** Colorimetric
888 quantification of NBT-formazan deposition in rosette leaves (see Methods). FW, fresh weight.
889 Data are means ± SD of three replicates (n=18). **(E)** Hydrogen peroxide (H_2O_2) content, quantified
890 as mmol H_2O_2 per gram dry weight (DW) of rosette leaves using the Amplex Red-coupled
891 fluorescence quantitative assay. Data are means ± SD of three replicates (n=14). **(F)** Ectopic cell
892 death detected by Trypan blue staining (see Methods). Data are means ± SD of three replicates
893 (n=7-10). **(G)** Elevation of transcripts in *MSL10-GFP* overexpression lines is suppressed by high
894 temperature. RNA extraction, cDNA synthesis, and qRT-PCR analyses in **(B)** and **(G)** were
895 performed as in Figure 2.
896
897 **Figure 4. Phospho-mimetic substitutions in the MSL10 N-terminus suppress phenotypes**
898 **associated with overexpression of MSL10^{S640L}. (A) Top row:** Images of three-week-old plants
899 grown at 21°C overexpressing wild-type *MSL10-GFP,* phospho-mimetic *MSL10^{7D}-GFP,*
900 *MSL10^{S640L}-GFP*, or *MSL10^{7D,S640L}-GFP*. Overexpression lines were generated in the *msl9-*
901 *1;msl10-1* background, phenotypically indistinguishable from *msl10-1*. Two independent
902 homozygous T3 lines for each transgene are shown. Bar = 0.5 cm. **Middle row:** Trypan blue
903 staining of four-week old leaves from the above T3 plants to visualize ectopic cell death. **Bottom**
904 **row**: DAB staining of five-week-old leaves to detect the accumulation of H_2O_2. For leaf images,
905 bar = 0.2 mm. **(B)** Immunoblot showing that plants harboring various *MSL10-GFP* transgenes
906 accumulate MSL10-GFP to similar levels. Western blot performed as in Figure 3C. The two forms
907 of MSL10-GFP that migrate slower on SDS-PAGE may result from posttranslational
908 modifications.
909

910 **Figure 5. The soluble N- and C- termini of MSL10 interact. (A)** Split ubiquitin yeast two-
911 hybrid assay. The strength of interaction between MSL10 truncations was determined in liquid
912 assays (see Methods). The NubWT moiety is used as a positive control. Data presented are means
913 ± SD of three replicates. Different letters indicate significant differences as determined by one-
914 way ANOVA followed by Tukey's post-hoc test ($P < 0.05$). **(B)** Confocal laser scanning
915 micrographs of the abaxial surface of *N. benthamiana* leaves 3 to 5 days after infiltration with
916 *Agrobacterium* harboring the indicated BiFC construct pairs. Scale bar, 50 µm. Identical
917 acquisition settings were used in all images. All experiments were repeated at least three times.
918 MSL10* indicates $MSL10^{S640L}$.
919
920 **Figure 6. Transcriptome profiling identifies downstream genes associated with *MSL10* gain-**
921 **of-function lines**. **(A)** Overview of our experimental approach. (**B)** Averaged expression profiles
922 of gene clusters were identified by centroid based *k*-means clustering using a *K*-means function in
923 R. The $\log_2$-transformed expression levels are plotted on the y-axis and samples with biological
924 replicates on the x-axis. **(C)** The top seven Gene Ontology classes of genes belonging to Cluster
925 2 as determined through the PANTHER statistical overrepresentation test. The number of genes
926 corresponding to each overrepresented GO term and its associated *p* values are shown. **(D)** Five
927 genes selected from the *MSL10-GFP* overexpression RNA-Seq Cluster 2 were upregulated in
928 *MSL10-GFP* overexpression lines, the *msl10-3G* mutant, and lines expressing the $MSL10g^{7A}$
929 transgene. RNA extraction, cDNA synthesis, and qRT-PCR analyses were performed as in **Figure**
930 **3.** Plants were grown at 21°C under 24-h of light.
931
932 **Figure 7. A three-step model for the regulation of MSL10's cell death signaling function**
933 For simplicity, only the soluble N- and C-terminal domains of MSL10 are shown. They could be
934 from the same or from different monomers. The inactive N-terminus, active N-terminus, and C-
935 terminus are represented by rectangles colored blue, red, and green, respectively. Proposed
936 conformational changes are indicated by changes in the shape of each rectangle. This model
937 explains the signaling output (red arrow) observed in wild type plants **(A)**, in response to MSL10-
938 GFP overexpression **(B)**, in the presence of MSL10 phospho-variants **(C)**, in the presence of alleles
939 or transgenes harboring the S640L mutation in the C-terminus (**D**, top), or in the presence of a

940 transgene that combines S640L with phospho-mimetic substitutions in the N-terminus (**D**,
941 bottom).
942
943 **Supplemental Figure 1. *msl10-3G* is a recessive gain-of-function allele.**
944 **(A)** Representative images of parental and F1 offspring plants from a *msl10-3G* backcross to wild
945 type *Col-0*. Top, four-week-old; bottom, eight-week-old plants. Bar = 0.5 cm. **(B)** Representative
946 images of parental and F1 offspring from a *msl10-3G* outcross to *msl10-1*. Top, four-week-old
947 plants; bottom, twelve-week-old plants. Bar = 0.5 cm. **(C)** Table showing segregation of *msl10-*
948 *3G* inheritance data compared to the expected ratios using a chi-squared analysis. Plants were
949 randomly chosen for genotyping.
950
951 **Supplemental Figure 2. *msl10-3G* allele and *MSL10g^{7A}* transgene exhibit similar reduction**
952 **in fresh weight, petiole length, plant height and apical dominance to *35S:MSL10-GFP***
953 **(A)** Relative transcript abundance of *MSL10* in the indicated lines. Left panel displays
954 accumulation of *MSL10* transcripts in plants harboring the *35S:MSL10-GFP* transgene, genomic
955 *MSL10g* phospho-variants, the EMS-induced point mutant allele *msl10-3G* or the null mutant
956 allele *msl10-1* compared to wild-type *Col-0*. Right panel depicts *MSL10* expression only in wild
957 type, null mutant allele and genomic *MSL10g* phospho-variants. cDNA was synthesized from total
958 RNA extracted from rosette leaves of three-week-old plants. Expression levels of respective genes
959 were analyzed with qRT-PCR and normalized to both *EF1α* and *UBQ5*. Mean fold-change values
960 relative to the wild type are plotted, with error bars showing ±SE of the mean of three biological
961 replicates. **(B)** Average fresh weight of rosettes clipped from three-week-old plants of the indicated
962 genotypes. Error bars indicate ±SD of three replicates (n=10 per replicate). **(C)** Plant height
963 measurement from eight-week-old plants from indicated genotypes. Error bars indicate ±SD of
964 three replicates (n=20-30 per replicate). Different letters indicate significant difference as
965 determined by one-way ANOVA followed by Scheffe's post-hoc test ($P < 0.05$) for unbalanced
966 samples. **(D)** Representative images of eight-week-old adult plants from indicated genotypes. **(E)**
967 Leaf blade length of seventh leaf from 35-day-old plants from the indicated genotypes. Error bars
968 indicate ±SD of three replicates (n=18 per replicate). **(F)** Leaf blade width of fourth or fifth leaf
969 from 35-day-old plants from the indicated genotypes. Error bars indicate ±SD of three replicates
970 (n=18 per replicate). **(G)** Average number of floral apices were counted from six to seven-week-

971 old plants of the indicated genotypes. Error bars indicate ±SD of three replicates (n=20 per
972 replicate). The T4 homozygous transgenic lines expressing either *35S:MSL10-GFP* in *Col-0*
973 background (*15-2*) and T3 homozygous transgenic lines expressing *MSL10g*, or *MSL10g*^{7D} in the
974 *msl10-1* background, and T3 segregating or T3 homozygous lines for *MSL10g*^{7A} were selected for
975 comparison. Plants of indicated genotypes were grown side-by-side in soil at 21°C under a 24- h
976 light regime. Different letters indicate significant differences, as determined by one-way ANOVA
977 followed by Tukey's post-hoc test ($P < 0.05$).
978
979 **Supplemental Figure 3. DEX-inducible overexpression of *MSL10* and *MSL10*^{4A} promotes the**
980 **upregulation of MSL10-associated marker genes and ectopic cell death**. Representative
981 images of five-week old plants grown under a short-day photoperiod (10 h light/14 h dark) sprayed
982 with 0.016% ethanol (mock; top row) or 30 µM DEX (bottom row) for 5 days. Expression profiles
983 of five marker genes before and after DEX treatment of transgenic plants expressing *DEX:MSL10*
984 and its phospho-variants using semi-quantitative RT-PCR. Rosette leaves from five-week-old
985 plants were infiltrated with 10 µM DEX or mock (0.016% ethanol), and tissue was harvested 12 h
986 post infiltration. Total RNA was isolated from *Col-0*, and from two independent homozygous T3
987 lines expressing either *DEX:MSL10*, *DEX:MSL10*^{4A} or *DEX:MSL10*^{4D}. Expression of *UBQ5* was
988 used as a control.
989
990 **Supplemental Figure 4. Growth at elevated temperature rescues the whole plant phenotypes**
991 **associated with overexpression of *MSL10-GFP*. (A)** Comparison of average fresh weight of
992 rosettes clipped from three-week-old plants of the indicated genotypes grown side-by-side at 21°C
993 or 28-30°C under a 24-h light regime. Error bars indicate SD of three replicates (n=10 per
994 replicate). FW= fresh weight. **(B)** Confocal images of epidermal cells showing GFP signal from
995 three-week-old plants of indicated genotypes. WT was used as a background control. T4
996 homozygous transgenic lines overexpressing *MSL10-GFP* were used.
997
998 **Supplemental Figure 5. High temperature suppresses the accumulation of H_2O_2 and the**
999 **incidence of ectopic cell death associated with *MSL10* gain-of function lines.** Leaves from
1000 three-week-old plants from each line grown either at 21°C (top row) or at an elevated temperature
1001 of 28-30°C (bottom row) under 24-h light regime were used for the experiment. Three independent

1002 T3 homozygous transgenic lines expressing *MSL10g, MSL10g*^{7A} or *MSL10g*^{7D} in the *msl10-1*
1003 background were selected for comparison. **(A)** Elevated levels of H_2O_2 detected by DAB staining.
1004 Representative bright-field images of rosette leaves are shown. Bar = 200 µm. **(B)** Visualization
1005 of ectopic cell death incidence by Trypan blue staining. Bar = 200 µm.
1006
1007 **Supplemental Figure 6. Growth retardation, accumulation of ROS and incidence of ectopic**
1008 **cell death associated with expression of the *MSL10g*^{7A} transgene and the *msl10-3G* allele were**
1009 **suppressed by growth at high temperature.** Three independent T3 homozygous transgenic lines
1010 expressing *MSL10g*, *MSL10g*^{7A}, or *MSL10g*^{7D} in the *msl10-1* background were selected for
1011 comparison. Plants of indicated genotypes were grown side-by-side on soil under a 24 h light
1012 regime at either 21°C or 28°-30°C. Different letters indicate significant differences, as determined
1013 by two-way ANOVA followed by Tukey's post-hoc test ($P < 0.05$). **(A)** Morphological phenotypes
1014 of four-week-old plants of the indicated genotypes. Bar = 0.5 cm. **(B)** Plant height of the indicated
1015 genotypes. Data are means ± SD of three replicates (n=15-18). **(C)** Whole-plant images of eight-
1016 week-old plants of the indicated genotypes. Bar = 0.5 cm. **(D)** Colorimetric quantification of NBT-
1017 formazan deposition on rosette leaves. FW, fresh weight. Data are means ± SD of three replicates
1018 (n=18). **(E)** Hydrogen peroxide (H_2O_2) content, quantified as the H_2O_2 (mmol) per gram dry
1019 weight (DW) of rosette leaves using Amplex Red-coupled fluorescence quantitative assay. Values
1020 are means ± SD of three replicates (n=14). **(F)** Quantification of ectopic cell death detected by
1021 Trypan blue staining. Data are means ± SD of three replicates each one consisting of 7 to 10 leaves.
1022 **(G)** Semi-quantitative RT-PCR analysis of *MSL10* from lines expressing *MSL10g* transgene or its
1023 phospho-variants and *msl10-3G* lesion. cDNA was synthesized from total RNA extracted from
1024 three-week-old plants of the indicated genotypes. *EF1α* was used as a loading control.
1025
1026 **Supplemental Figure 7. Additional controls for the BiFC assay. (A)** The C-terminal half of
1027 MSL10 forms aggregates when fused to GFP. Representative confocal images of abaxial *N.*
1028 *benthamiana* leaf epidermis from plants transiently expressing truncated $MSL10_{461\text{-}734}$-GFP and
1029 MSL10 $^{S640L}{}_{461\text{-}734}$-GFP. Images were taken 5 d post-infiltration. Scale bar, 50 µm. **(B)** *N.*
1030 *benthamiana* leaves co-infiltrated with constructs fused to the split YFP were observed under the
1031 confocal microscope 3-5 days after infiltration. Scale bar, 50 µm. (**Top row**) Neither domain
1032 interacts with KAT1. (**Middle row**) Neither phosphorylation status of the N-terminus nor the

1033 S640L lesion in the C-terminus affect the interaction. either reconstituted YFP fluorescence signal
1034 from positive interaction or marked reduction in YFP signal in case of negative interaction from
1035 indicated combinations. (Bottom row) Negative controls for the N-terminus with the S640L lesion.
1036 Scale bar, 50 µm.
1037
1038 **Supplemental Figure 8. Analysis of reliability of RNA-seq samples using multi-dimensional**
1039 **scaling plot (MDS) and correlation between RNA-seq and qRT-PCR derived expression**
1040 **data**. **(A)** MDS plot indicates biological variation across treatments and genotypes. MDS plot was
1041 generated using edgeR (Robinson et al., 2010). FC, Fold change; dim, dimension. **(B)** Table
1042 showing the list of hallmark genes associated with *MSL10* gain-of-function lines that are also
1043 identified in the RNA-seq analysis.
1044
1045 **Supplemental Table 1.** mRNA sequencing and alignment statistics
1046
1047 **Supplemental Table 2. List of differentially expressed genes identified in the transcriptomic**
1048 **analysis belonging to Cluster 2.** Marked in yellow are the two columns corresponding to the two
1049 replicates of *35S:MSL10-GFP* overexpression lines grown at 21°C.
1050
1051 **Supplemental Table 3. Tabulated list of overrepresented GO terms (biological process) and**
1052 **corresponding P values from the enrichment analysis performed using the PANTHER**
1053 **classification tool**
1054
1055 **Supplemental Table 4. List of selected genes with threshold value >10 and significantly**
1056 **enriched in at least two overrepresented GO categories.** Marked in yellow are the two columns
1057 corresponding to the two replicates of *35S:MSL10-GFP* overexpression lines grown at 21°C.
1058 Marked in green are the genes selected for qRT-PCR in this study.
1059
1060 **Supplemental Table 5**. List of primers used in this study.